J. Fluid Mech. (2023), *vol*. 954, A36, doi:10.1017/jfm.2022.878

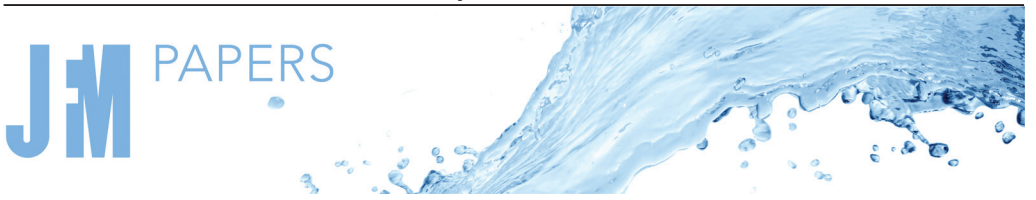

Evolution of dissipative fluid flows with imposed helicity conservation

Zhaoyuan Meng[1], **Weiyu Shen**[1] **and Yue Yang**[1,2],†

[1]State Key Laboratory for Turbulence and Complex Systems, College of Engineering, Peking University, Beijing 100871, PR China

[2]HEDPS-CAPT, Peking University, Beijing 100871, PR China

(Received 3 June 2022; revised 1 September 2022; accepted 16 October 2022)

We propose the helicity-conserved Navier–Stokes (HCNS) equation by modifying the non-ideal force term in the Navier–Stokes (NS) equation. The corresponding HCNS flow has strict helicity conservation, and retains major NS dynamics with finite dissipation. Using the helical wave decomposition, we show that the pentadic interaction of Fourier helical modes in the HCNS dynamics is more complex than the triadic interaction in the NS dynamics, and enhanced variations for left- and right-handed helicity components cancel each other in the HCNS flow to keep the invariant helicity. A comparative study of HCNS and NS flow evolutions with direct numerical simulation elucidates the influence of the helicity conservation on flow structures and statistics in the vortex reconnection and isotropic turbulence. First, the HCNS flow evolves towards a Beltrami state with a -4 scaling law of the energy spectrum at high wavenumbers at long times. Second, large-scale flow structures are almost identical during the viscous reconnection of vortex tubes in the two flows, whereas many more small-scale helical structures are generated via the pentadic mode interaction in the HCNS flow than in the NS flow. Moreover, we demonstrate that parity breaking at small scales can trigger a notable helicity variation in the NS flow. These findings hint that the helicity may not be conserved in the inviscid limit of the NS flow.

Key words: topological fluid dynamics, vortex dynamics, isotropic turbulence

1. Introduction

Helicity (Moreau 1961; Moffatt 1969; Arnold 2014) is an important global quantity describing the topology of a divergence-free vector field. Intuitively, a flow field with a non-zero helicity can have helical stream or vortex lines. Typical vortex tubes with an axial flow and non-zero helicity were reported in wing-tip vortices (Devenport *et al.* 1996; Tong, Yang & Wang 2020), Taylor–Görtler vortices (Wood, Mehta & Koh 1992), streamwise

† Email address for correspondence: yyg@pku.edu.cn

vortices in shear flows (Hall & Sherwin 2010; Zhao, Yang & Chen 2016; Ruan *et al.* 2022), tornadoes (Kurgansky 2017), Langmuir circulations (Moffatt & Tsinober 1992) and helical coherent structures in turbulence (Tsinober & Levich 1983; Hussain 1986; Pelz, Shtilman & Tsinober 1986; Xiong & Yang 2019*a*).

In particular, helicity is one of only two quadratic invariants in three-dimensional ideal fluid flows (the other one is kinetic energy). It plays an essential role in the generation and energy cascade of turbulent flows (Arnold 1992; Moffatt & Tsinober 1992; Moffatt 2021). André & Lesieur (1977) showed that a finite helicity can be generated from an initial state with vanishing helicity in decaying isotropic turbulence at high Reynolds numbers, illustrating the prevalence of helicity in turbulent flows. Moffatt (2014) and Alexakis & Biferale (2018) pointed out that helicity can impede the forward energy cascade and even promote the inversion of energy transfer.

Unlike kinetic energy, helicity is not sign definite and its sign is changed by altering the chirality of the coordinate frame. Therefore, helicity is a pseudo-scalar and characterizes the parity breaking of a fluid flow. The parity can be quantified by the helical wave decomposition (HWD) (Constantin & Majda 1988; Waleffe 1992). Using the HWD, Chen, Chen & Eyink (2003*a*) and Chen *et al.* (2003*b*) studied the joint cascade of energy and helicity in three-dimensional turbulence, and conjectured the asymptotic restoration of parity symmetry at small scales. Yang, Su & Wu (2010) and Yang & Wu (2011) extended the HWD to an arbitrary single-connected domain. Zhu, Yang & Zhu (2014) studied purely helical absolute equilibria of incompressible turbulence with the HWD. Alexakis (2017) investigated the interaction between different helical modes in turbulent flows, based on a decomposition of energy and helicity fluxes. Yan *et al.* (2020) proposed the dual-channel helicity cascade as a mechanism of hindered or inverse energy cascade. However, the specific role of helicity in three-dimensional turbulence remains an open problem (Chen *et al.* 2003*a*; Yao & Hussain 2022).

Since helicity can vary in viscous flows, its dynamics has been extensively investigated during topological change, e.g. viscous reconnection (Kida & Takaoka 1994; Yao & Hussain 2022), of a trefoil knotted vortex tube with simple initial geometry and non-trivial topology in numerical simulations (e.g. Kida & Takaoka 1987; Ricca, Samuels & Barenghi 1999; Scheeler *et al.* 2014; Kerr 2018; Xiong & Yang 2019*a*; Yao, Yang & Hussain 2021; Zhao *et al.* 2021; Shen *et al.* 2022) and experiments (e.g. Kleckner & Irvine 2013; Scheeler *et al.* 2014). Kida & Takaoka (1987, 1988) reported that helicity decays in the entire evolution at a low Reynolds number $Re = 1200$, and the decay rate decreases with increasing Re, implying that helicity may be conserved in the inviscid limit. By contrast, the recent direct numerical simulation (DNS) of trefoil vortex knots (Yao *et al.* 2021; Zhao & Scalo 2021; Zhao *et al.* 2021) and Hopf links (Yao *et al.* 2022) at high Reynolds numbers found a 'transient growth' of helicity when vortex reconnection occurs, implying that helicity is not conserved in the inviscid limit. Since helicity and its time derivative are not positive definite, the study of helicity in limiting conditions appears to be more challenging than that of kinetic energy or the mean dissipation rate (Batchelor 1953; Sreenivasan 1984, 1998; Kaneda *et al.* 2003). Thus, there is no consensus on whether helicity is conserved in the inviscid limit (Moffatt 2017; Yao & Hussain 2022). This open problem inspires us to think from another perspective – how does the flow evolution change if we impose helicity conservation on the Navier–Stokes (NS) equations?

The NS equations were modified to understand some specific roles of helicity. Biferale, Musacchio & Toschi (2012, 2013) performed a surgery of the NS dynamics by only keeping the velocity components carrying a well-defined positive or negative helicity, and then they found a stationary inverse energy cascade in homogeneous isotropic

turbulence (HIT). Biferale & Titi (2013) then demonstrated the global regularity of such helical-decimated NS equations. Furthermore, a series of studies explored the relation between helicity and the direction of energy cascade (e.g. Sahoo, Alexakis & Biferale 2017; Slomka & Dunkel 2017; Alexakis & Biferale 2018; Plunian *et al.* 2020; Alexakis & Biferale 2022). Hao, Xiong & Yang (2019) applied vorticity-based orthogonal decomposition to the non-ideal force in the NS equations, and showed that vortex surfaces can be tracked by a virtual velocity in the modified fluid flow with helicity conservation. She & Jackson (1993) and Gallavotti (1996, 1997) discussed another approach to modify the NS equations by introducing integral constraints with a Lagrange multiplier. In this way, the constrained Euler equation (She & Jackson 1993) and the Gaussian dissipative Euler equation (Gallavotti 1997) with conserved kinetic energy, and the Gaussian NS equation (Gallavotti 1996, 1997; Jaccod & Chibbaro 2021) with conserved enstrophy were obtained. In addition, Bos (2021) kept the enstrophy conserved in turbulence by removing vortex stretching from the NS equations.

In the present study, we investigate the influence of helicity on vortex dynamics and flow statistics by imposing helicity conservation on the NS equations while retaining major NS dynamics. The modified NS equation is referred to as the helicity-conserved Navier–Stokes (HCNS) equation. We then compare the evolutions governed by NS and HCNS equations in various flows to reveal the critical role of helicity. Moreover, the HWD is used to explore the relation between small-scale parity breaking and large-scale helical structures. These efforts can explain the transient helicity variation during vortex reconnection and facilitate flow control by manipulating small-scale flow structures.

The outline of the present paper is as follows. Section 2 introduces the HCNS equation and derives the properties of the HCNS flow. Section 3 studies the HWD of NS and HCNS dynamics. Section 4 describes numerical set-ups and methods. Section 5 compares evolutions of vortical structures and flow statistics in HCNS and NS flows. Some conclusions are drawn in § 6.

2. Theoretical framework of the HCNS flow

2.1. *Introduction of the HCNS equation*

In a three-dimensional incompressible flow, the velocity $\boldsymbol{u}(\boldsymbol{x}, t)$ is governed by the NS equations

$$\boldsymbol{\nabla} \cdot \boldsymbol{u} = 0, \tag{2.1}$$

$$\frac{\partial \boldsymbol{u}}{\partial t} + \boldsymbol{\omega} \times \boldsymbol{u} = -\boldsymbol{\nabla} P + \boldsymbol{F}, \tag{2.2}$$

where $\boldsymbol{\omega} \equiv \boldsymbol{\nabla} \times \boldsymbol{u}$ is the vorticity, $P = p/\rho + |\boldsymbol{u}|^2/2 + V_F$ denotes a generalized potential with the pressure p, density ρ and potential V_F of conservative body forces and

$$\boldsymbol{F} = \frac{1}{\rho}\boldsymbol{\nabla} \cdot \boldsymbol{\tau} + \boldsymbol{f} \tag{2.3}$$

denotes a generalized non-ideal force with viscous stress $\boldsymbol{\tau}$ and non-conservative external body force $\boldsymbol{f}$ per unit mass. Note that it is straightforward to extend the present analysis to compressible flows (Hao *et al.* 2019).

From (2.2), we obtain the vorticity equation

$$\frac{\partial \boldsymbol{\omega}}{\partial t} + \nabla \times (\boldsymbol{\omega} \times \boldsymbol{u}) = \nabla \times \boldsymbol{F}, \tag{2.4}$$

and then the transport equation

$$\frac{\partial h}{\partial t} + \nabla \cdot [P\boldsymbol{\omega} + \boldsymbol{u} \times (\boldsymbol{u} \times \boldsymbol{\omega}) + \boldsymbol{u} \times \boldsymbol{F}] = 2\boldsymbol{\omega} \cdot \boldsymbol{F} \tag{2.5}$$

of the helicity density $h \equiv \boldsymbol{u} \cdot \boldsymbol{\omega}$.

We impose helicity conservation on the NS equations by modifying the non-ideal force in (2.2), where the helicity (Moreau 1961; Moffatt 1969)

$$\mathcal{H}(t) \equiv \int_{\mathcal{D}} h \, \mathrm{d}V \tag{2.6}$$

is defined over an unbounded domain $\mathcal{D}$ or that bounded by a vortex surface. To remove the source term of helicity generation, i.e. the right-hand side of (2.5), we apply the vorticity-based orthogonal decomposition (Hao *et al.* 2019) to

$$\boldsymbol{F} = \boldsymbol{F}_{\perp} + \boldsymbol{F}_{\parallel} = (\boldsymbol{n}_{\omega} \times \boldsymbol{F}) \times \boldsymbol{n}_{\omega} + (\boldsymbol{n}_{\omega} \cdot \boldsymbol{F})\boldsymbol{n}_{\omega}, \tag{2.7}$$

and only keep the orthogonal component $\boldsymbol{F}_{\perp} = (\boldsymbol{n}_{\omega} \times \boldsymbol{F}) \times \boldsymbol{n}_{\omega}$ with $\boldsymbol{n}_{\omega} \equiv \boldsymbol{\omega}/|\boldsymbol{\omega}|$ in $\boldsymbol{F}$ in (2.2). To avoid the issue of singularity, we define $\boldsymbol{n}_{\omega} = \boldsymbol{0}$ and $\boldsymbol{F}_{\perp} = \boldsymbol{F}$ at the points with $|\boldsymbol{\omega}| = 0$.

Thus, we obtain the HCNS equation

$$\frac{\partial \boldsymbol{u}}{\partial t} + \boldsymbol{\omega} \times \boldsymbol{u} = -\nabla P + (\boldsymbol{n}_{\omega} \times \boldsymbol{F}) \times \boldsymbol{n}_{\omega}, \tag{2.8}$$

and the corresponding vorticity equation

$$\frac{\partial \boldsymbol{\omega}}{\partial t} + \nabla \times (\boldsymbol{\omega} \times \boldsymbol{u}) = \nabla \times [(\boldsymbol{n}_{\omega} \times \boldsymbol{F}) \times \boldsymbol{n}_{\omega}], \tag{2.9}$$

for the HCNS flow governed by (2.8) and (2.1). Note that the HCNS equation degenerates to the NS equation in one and two dimensions, and it has all the symmetry groups (Frisch 1995) of the NS equation.

2.2. *Evolution of integral quantities for the HCNS flow*

Without loss of generality, we consider viscous, barotropic and incompressible fluid flows without body forces, i.e. $P = p/\rho + |\boldsymbol{u}|^2/2$ and $\boldsymbol{F} = \nu\nabla^2\boldsymbol{u}$ with kinematic viscosity ν below. The corresponding momentum and vorticity equations for the HCNS flow are

$$\frac{\partial \boldsymbol{u}}{\partial t} + \boldsymbol{\omega} \times \boldsymbol{u} = -\nabla P + \nu(\boldsymbol{n}_{\omega} \times \nabla^2\boldsymbol{u}) \times \boldsymbol{n}_{\omega} \tag{2.10}$$

and

$$\frac{\partial \boldsymbol{\omega}}{\partial t} + \nabla \times (\boldsymbol{\omega} \times \boldsymbol{u}) = \nu\nabla \times [(\boldsymbol{n}_{\omega} \times \nabla^2\boldsymbol{u}) \times \boldsymbol{n}_{\omega}], \tag{2.11}$$

respectively. Next, we derive transport equations of the total kinetic energy

$$E(t) \equiv \int_{\mathcal{D}} \frac{|\boldsymbol{u}|^2}{2} \, \mathrm{d}V, \tag{2.12}$$

enstrophy

$$\Omega(t) \equiv \int_{\mathcal{D}} \frac{|\boldsymbol{\omega}|^2}{2}\,\mathrm{d}V \tag{2.13}$$

and helicity (2.6) for the HCNS flow.

First, the transport equation of the local kinetic energy reads

$$\frac{\mathrm{D}}{\mathrm{D}t}\frac{|\boldsymbol{u}|^2}{2} = \boldsymbol{\nabla}\cdot\left(-\frac{p}{\rho}\boldsymbol{u} + \nu\boldsymbol{u}\times\boldsymbol{\omega}\right) - \nu|\boldsymbol{\omega}|^2 + \nu h\xi_\omega. \tag{2.14}$$

Here, $\mathrm{D}/\mathrm{D}t \equiv \partial/\partial t + \boldsymbol{u}\cdot\boldsymbol{\nabla}$ is the material derivative and $\xi_\omega \equiv \boldsymbol{n}_\omega\cdot(\boldsymbol{\nabla}\times\boldsymbol{n}_\omega)$ denotes the torsion of neighbouring vortex lines (Truesdell 2018). Integrating (2.14) over $\mathcal{D}$ yields

$$\frac{\mathrm{d}E}{\mathrm{d}t} = -2\nu\Omega + \nu\int_{\mathcal{D}}\xi_u\xi_\omega|\boldsymbol{u}|^2\,\mathrm{d}V, \tag{2.15}$$

where $\xi_u \equiv \boldsymbol{n}_u\cdot(\boldsymbol{\nabla}\times\boldsymbol{n}_u)$, similar to ξ_ω, denotes the torsion of neighbouring streamlines with $\boldsymbol{n}_u \equiv \boldsymbol{u}/|\boldsymbol{u}|$. Note that our discussion is restricted to an unbounded domain or a periodic domain $\mathcal{D}$, otherwise there will be a boundary integral term in (2.15).

We demonstrate that the HCNS flow is dissipative, i.e. $\mathrm{d}E/\mathrm{d}t \le 0$. Considering $\xi_u(\boldsymbol{x})\xi_\omega(\boldsymbol{x})$ is a continuous function and $|\boldsymbol{u}(\boldsymbol{x})|^2 \ge 0$ within $\mathcal{D}$, applying the mean value theorem for integrals to (2.15) yields

$$\frac{\mathrm{d}E}{\mathrm{d}t} = -2\nu\Omega + 2\nu\xi_u^*\xi_\omega^* E, \tag{2.16}$$

with $\xi_u^* = \xi_u(\boldsymbol{x}^*)$ and $\xi_\omega^* = \xi_\omega(\boldsymbol{x}^*)$ at a particular $\boldsymbol{x}^*$ in $\mathcal{D}$.

For a periodic cube $\mathcal{D}$, comparing Fourier expansions of E and Ω yields

$$\Omega = \frac{L^3}{2}\sum_{\boldsymbol{k}} k^2|\hat{\boldsymbol{u}}|^2 \ge q_0^2\frac{L^3}{2}\sum_{\boldsymbol{k}}|\hat{\boldsymbol{u}}|^2 = q_0^2 E, \tag{2.17}$$

where L denotes the side length of $\mathcal{D}$, $\boldsymbol{k}$ the wavenumber vector, $k \equiv |\boldsymbol{k}|$ the wavenumber magnitude and $\hat{\boldsymbol{u}} = \hat{\boldsymbol{u}}(\boldsymbol{k}, t)$ the velocity component in Fourier space. In general, we have $q_0 \gg 1$ due to the weight k^2 in (2.17), unless the energy spectrum is only non-vanishing at several lowest wavenumbers in a simple flow, e.g. the Taylor–Green initial field (Taylor & Green 1937) with the energy spectrum as a Delta-function. Substituting (2.17) with $q_0 \gg 1$, $|\xi_u^*| = O(1)$ and $|\xi_\omega^*| = O(1)$ into (2.16) yields that the HCNS flow is dissipative as

$$\frac{\mathrm{d}E}{\mathrm{d}t} \le -2\nu\Omega + 2\nu|\xi_u^*||\xi_\omega^*|E \le 2\nu\Omega\left(\frac{|\xi_u^*||\xi_\omega^*|}{q_0^2} - 1\right) \le 0. \tag{2.18}$$

Second, we consider the transport of enstrophy. Taking inner product of (2.11) with $\boldsymbol{\omega}$ yields

$$\frac{\mathrm{D}}{\mathrm{D}t}\frac{|\boldsymbol{\omega}|^2}{2} = \boldsymbol{\omega}\cdot\boldsymbol{S}\cdot\boldsymbol{\omega} + \nu\left\{-\sin^2\vartheta_\omega|\nabla^2\boldsymbol{u}|^2 + \boldsymbol{\nabla}\cdot[\boldsymbol{\omega}\times(\boldsymbol{\nabla}\times\boldsymbol{\omega})]\right\}, \tag{2.19}$$

where $\boldsymbol{S} \equiv (\boldsymbol{\nabla}\boldsymbol{u} + \boldsymbol{\nabla}\boldsymbol{u}^T)/2$ is the rate-of-strain tensor and

$$\vartheta_\omega \equiv \arccos\frac{\boldsymbol{\omega}\cdot\nabla^2\boldsymbol{u}}{|\boldsymbol{\omega}||\nabla^2\boldsymbol{u}|} \tag{2.20}$$

denotes the angle between $\boldsymbol{\omega}$ and $\nabla^2\boldsymbol{u}$. Compared with the NS flow, the prefactor $0 \le \sin^2\vartheta_\omega \le 1$ of the second term on the right-hand side of (2.19) weakens the enstrophy dissipation in the HCNS flow (Hao *et al.* 2019).

By integrating (2.19) over $\mathcal{D}$, we obtain

$$\frac{\mathrm{d}\Omega}{\mathrm{d}t} = \mathcal{P}_\Omega - \mathcal{E}_\Omega^{\mathrm{HCNS}}, \tag{2.21}$$

after some algebra, with the production term

$$\mathcal{P}_\Omega = \int_{\mathcal{D}} \nabla^2 \boldsymbol{u} \cdot (\boldsymbol{\omega} \times \boldsymbol{u}) \,\mathrm{d}V \tag{2.22}$$

and the dissipation term

$$\mathcal{E}_\Omega^{\mathrm{HCNS}} = \nu \int_{\mathcal{D}} \sin^2 \vartheta_\omega |\nabla^2 \boldsymbol{u}|^2 \,\mathrm{d}V. \tag{2.23}$$

Comparing $\mathcal{E}_\Omega^{\mathrm{HCNS}}$ in the HCNS flow and

$$\mathcal{E}_\Omega^{\mathrm{NS}} = \nu \int_{\mathcal{D}} |\nabla^2 \boldsymbol{u}|^2 \,\mathrm{d}V \tag{2.24}$$

in the NS flow, we have $\mathcal{E}_\Omega^{\mathrm{HCNS}} \leq \mathcal{E}_\Omega^{\mathrm{NS}}$ with identical production terms in the two flows. Hence, the integration of (2.21) with time from the same initial condition suggests that

$$\Omega^{\mathrm{HCNS}}(t) \geq \Omega^{\mathrm{NS}}(t), \tag{2.25}$$

where the superscripts 'NS' and 'HCNS' denote the quantities in NS and HCNS flows, respectively.

Finally, the general equation (2.5) for the helicity density becomes

$$\frac{\mathrm{D}h}{\mathrm{D}t} = \boldsymbol{\nabla} \cdot [P'\boldsymbol{\omega} - \nu \boldsymbol{u} \times \nabla^2 \boldsymbol{u} + \nu(\boldsymbol{n}_\omega \cdot \nabla^2 \boldsymbol{u})\boldsymbol{u} \times \boldsymbol{n}_\omega] \tag{2.26}$$

in the HCNS flow, where $P' \equiv -p/\rho + |\boldsymbol{u}|^2/2$ denotes a modified pressure. Applying the divergence theorem to (2.26) yields

$$\frac{\mathrm{d}\mathcal{H}}{\mathrm{d}t} = \oiint_{\partial\mathcal{D}} \boldsymbol{n} \cdot [P'\boldsymbol{\omega} - \nu \boldsymbol{u} \times \nabla^2 \boldsymbol{u} + \nu(\boldsymbol{n}_\omega \cdot \nabla^2 \boldsymbol{u})\boldsymbol{u} \times \boldsymbol{n}_\omega] \,\mathrm{d}S. \tag{2.27}$$

Considering $\mathcal{D}$ with the vanishing boundary integral, (2.27) is simplified to

$$\frac{\mathrm{d}\mathcal{H}}{\mathrm{d}t} = 0. \tag{2.28}$$

Therefore, the HCNS flow has a strong constraint of helicity conservation:

$$\mathcal{H}(t) = \mathcal{H}_0, \quad \forall t \geq 0, \tag{2.29}$$

where the subscript '0' denotes a quantity at the initial time.

2.3. *Beltramization of the HCNS flow*

For a decaying HCNS flow, we show its Beltramization at long times with lower bounds of E and Ω, where a Beltrami flow has

$$\boldsymbol{\omega} = \lambda \boldsymbol{u}, \tag{2.30}$$

with a constant λ. Consider the Schwartz inequality

$$\mathcal{H}^2 \leq 4E\Omega, \tag{2.31}$$

for a velocity field with $\mathcal{H}_0 \neq 0$, which takes equal only for (2.30). From (2.29) and (2.31), we have

$$4E(t)\Omega(t) \geq \mathcal{H}_0^2 > 0, \tag{2.32}$$

which implies that both $E(t)$ and $\Omega(t)$ have non-vanishing lower bounds, otherwise one of them must diverge. Substituting (2.17) into (2.32) yields

$$\Omega \geq \frac{1}{2} q_0 |\mathcal{H}_0|. \tag{2.33}$$

Note that the HCNS flow allows both E and Ω to decay to zero for $\mathcal{H}_0 = 0$, e.g. for highly symmetric flows.

Next, we explore the Beltramization of HCNS flows at $t \to \infty$. First, the Beltrami field with (2.30) is a steady-state solution to the HCNS equation. For such a solution, (2.10) with $\boldsymbol{u}$, $\boldsymbol{\omega}$ and $\nabla^2 \boldsymbol{u}$ parallel to each other is simplified to $\partial \boldsymbol{u}/\partial t = \boldsymbol{0}$ with $\mathrm{d}E/\mathrm{d}t = 0$. Then, we demonstrate the Beltrami field with (2.30) represents the state of the lowest E in the HCNS flow using the variational principle (Woltjer 1958).

We seek the minimum E subject to the helicity conservation in (2.29). By varying a generic function

$$I_E \equiv \int_{\mathcal{D}} [\boldsymbol{u} \cdot \boldsymbol{u} - \lambda_E \boldsymbol{u} \cdot (\nabla \times \boldsymbol{u})] \, \mathrm{d}V, \tag{2.34}$$

for E, and applying the divergence theorem yield

$$\delta I_E = 2 \int_{\mathcal{D}} (\boldsymbol{u} - \lambda_E \nabla \times \boldsymbol{u}) \cdot \delta \boldsymbol{u} \, \mathrm{d}V + \oiint_{\partial \mathcal{D}} \lambda_E \boldsymbol{n} \cdot (\boldsymbol{u} \times \delta \boldsymbol{u}) \, \mathrm{d}S = 0, \tag{2.35}$$

with a Lagrangian multiplier λ_E. Since $\delta \boldsymbol{u}$ vanishes at $\partial \mathcal{D}$ for a closed domain $\mathcal{D}$, and the surface integral in (2.35) also vanishes for an unclosed domain such as the unbounded domain or periodic box, we obtain

$$\int_{\mathcal{D}} (\boldsymbol{u} - \lambda_E \nabla \times \boldsymbol{u}) \cdot \delta \boldsymbol{u} \, \mathrm{d}V = 0. \tag{2.36}$$

The vanishing integral (2.36) with an arbitrary $\delta \boldsymbol{u}$ suggests

$$\boldsymbol{u} = \lambda_E \nabla \times \boldsymbol{u}, \tag{2.37}$$

for the minimum E. Therefore, the Beltrami field with (2.30) and $\lambda = \lambda_E^{-1}$ corresponds to the lowest energy state of the HCNS flow. For the dissipative HCNS flow with (2.18) and

a non-vanishing lower bound of Ω in (2.33), the Beltrami flow is the only possible state at long times. At this state, the Schwartz inequality (2.31) becomes

$$4E_\infty \Omega_\infty = \mathcal{H}_0^2, \tag{2.38}$$

with $E_\infty = |\mathcal{H}_0|/(2|\lambda|)$ and $\Omega_\infty = |\lambda \mathcal{H}_0|/2$. The Beltramization of the HCNS flow can be characterized by the criterion

$$\Lambda_B(t) \equiv \frac{\mathcal{H}^2(t)}{4E(t)\Omega(t)} \in [0, 1]. \tag{2.39}$$

The Beltrami flow with (2.38) has $\Lambda_B = 1$.

3. The HWD of NS/HCNS dynamics

3.1. *The HWD*

Helicity is the signature of parity breaking in incompressible flows (Chen *et al.* 2003*a*), and the parity can be characterized by the HWD (Constantin & Majda 1988; Waleffe 1992). A divergence-free velocity field has $\boldsymbol{k} \cdot \hat{\boldsymbol{u}}(\boldsymbol{k}) = 0$, so $\hat{\boldsymbol{u}}(\boldsymbol{k})$ has two degrees of freedom. In the HWD, two independent degrees of freedom are obtained by projecting the velocity

$$\boldsymbol{u}(\boldsymbol{x}) = \sum_{\boldsymbol{k}} \hat{\boldsymbol{u}}(\boldsymbol{k})\, \mathrm{e}^{\mathrm{i}\boldsymbol{k}\cdot\boldsymbol{x}} = \sum_{\boldsymbol{k}} (u^+ \boldsymbol{h}^+ + u^- \boldsymbol{h}^-)\, \mathrm{e}^{\mathrm{i}\boldsymbol{k}\cdot\boldsymbol{x}} \tag{3.1}$$

onto two orthogonal helical waves with a definite sign of helicity. Here, $\boldsymbol{k} = (k_1, k_2, k_3)$ is for a periodic cube of side $L = 2\pi$, with $k_i = 0, \pm 1, \pm 2, \ldots, i = 1, 2, 3$. The helical modes $u^\pm(\boldsymbol{k})$ are complex scalars, and

$$\boldsymbol{h}^\pm(\boldsymbol{k}) = \frac{1}{\sqrt{2}} \frac{(\boldsymbol{z}_k \times \boldsymbol{k}) \times \boldsymbol{k}}{k|\boldsymbol{z}_k \times \boldsymbol{k}|} \pm \frac{\mathrm{i}}{\sqrt{2}} \frac{\boldsymbol{z}_k \times \boldsymbol{k}}{|\boldsymbol{z}_k \times \boldsymbol{k}|} \tag{3.2}$$

are two eigenvectors of the curl operator as $\mathrm{i}\boldsymbol{k} \times \boldsymbol{h}^\pm(\boldsymbol{k}) = \pm k \boldsymbol{h}^\pm(\boldsymbol{k})$, where $\boldsymbol{z}_k$ is randomly generated for each $\boldsymbol{k}$, keeping $|\boldsymbol{z}_k \times \boldsymbol{k}| \neq 0$. Note that $\boldsymbol{h}^+$ and $\boldsymbol{h}^-$ have properties $\boldsymbol{h}^\pm(\boldsymbol{k}) = \boldsymbol{h}^{\mp *}(\boldsymbol{k})$, $|\boldsymbol{h}^\pm|^2 = \boldsymbol{h}^+ \cdot \boldsymbol{h}^- = 1$ and $\boldsymbol{h}^+ \cdot \boldsymbol{h}^+ = \boldsymbol{h}^- \cdot \boldsymbol{h}^- = 0$, where the superscript '*' denotes the complex conjugate.

Projecting $\hat{\boldsymbol{u}}$ onto $\boldsymbol{h}^\mp$ yields

$$u^\pm(\boldsymbol{k}) = \hat{\boldsymbol{u}}(\boldsymbol{k}) \cdot \boldsymbol{h}^\mp(\boldsymbol{k}) = \frac{1}{L^3} \int_{L^3} \boldsymbol{h}^\mp(\boldsymbol{k}) \cdot \boldsymbol{u}(\boldsymbol{x})\, \mathrm{e}^{-\mathrm{i}\boldsymbol{k}\cdot\boldsymbol{x}}\, \mathrm{d}\boldsymbol{x}, \tag{3.3}$$

where u^+ and u^- are right- and left-handed components, respectively. The vorticity can also be expressed in terms of helical modes as

$$\hat{\boldsymbol{\omega}}(\boldsymbol{k}) = k(u^+(\boldsymbol{k})\boldsymbol{h}^+(\boldsymbol{k}) - u^-(\boldsymbol{k})\boldsymbol{h}^-(\boldsymbol{k})). \tag{3.4}$$

The integral quantities have HWDs

$$E(t) = E^+(t) + E^-(t), \quad \Omega(t) = \Omega^+(t) + \Omega^-(t), \quad \mathcal{H}(t) = \mathcal{H}^+(t) - \mathcal{H}^-(t), \tag{3.5a–c}$$

with

$$E^\pm \equiv \frac{L^3}{2} \sum_{\boldsymbol{k}} |u^\pm|^2, \quad \Omega^\pm \equiv \frac{L^3}{2} \sum_{\boldsymbol{k}} k^2 |u^\pm|^2, \quad \mathcal{H}^\pm \equiv L^3 \sum_{\boldsymbol{k}} k|u^\pm|^2. \tag{3.6a–c}$$

3.2. *Transient variation of helicity in the NS dynamics*

Applying the HWD with (3.1) and (3.3) to the NS equation (2.2) with $\boldsymbol{F} = \nu\nabla^2\boldsymbol{u}$ yields the equation for helical modes of velocity as (Waleffe 1992)

$$(\partial_t + \nu k^2)u^{s_k*}(\boldsymbol{k}, t) = -\frac{1}{2}\sum_{\boldsymbol{k}+\boldsymbol{p}+\boldsymbol{q}=\boldsymbol{0}}\sum_{s_p,s_q}(s_p p - s_q q)(\boldsymbol{h}^{s_k}\cdot\boldsymbol{h}^{s_p}\times\boldsymbol{h}^{s_q})u^{s_p}u^{s_q}. \tag{3.7}$$

There are eight helical combinations with $(s_k, s_p, s_q) = (\pm, \pm, \pm)$ among three interacting modes $u^{s_k}(\boldsymbol{k}, t)$, $u^{s_p}(\boldsymbol{p}, t)$ and $u^{s_q}(\boldsymbol{q}, t)$, and only four of them are independent due to parity symmetry.

Multiplying (3.7) by u^{s_k} and adding its complex conjugate, the evolution equation

$$(\partial_t + 2\nu k^2)|u^{s_k}|^2 = -\frac{1}{2}\sum_{\boldsymbol{k}+\boldsymbol{p}+\boldsymbol{q}=\boldsymbol{0}}\sum_{s_p,s_q}\mathcal{T}(\boldsymbol{k}, \boldsymbol{p}, \boldsymbol{q})u^{s_k}u^{s_p}u^{s_q} + \text{c.c.} \tag{3.8}$$

for the right- or left-handed energy component with

$$\mathcal{T}(\boldsymbol{k}, \boldsymbol{p}, \boldsymbol{q}) = (s_p p - s_q q)(\boldsymbol{h}^{s_k}\cdot\boldsymbol{h}^{s_p}\times\boldsymbol{h}^{s_q}) \tag{3.9}$$

is obtained, where c.c. denotes the complex conjugate. The right-hand side of (3.8) represents the inter-scale and inter-chiral energy transfer in the NS flow.

Multiplying (3.7) by u^{s_k}, adding its complex conjugate, swapping indices k, p, q and summing all of them up, we have

$$\frac{\partial}{\partial t}(|u^{s_k}|^2 + |u^{s_p}|^2 + |u^{s_q}|^2) = -2\nu(k^2|u^{s_k}|^2 + p^2|u^{s_p}|^2 + q^2|u^{s_q}|^2). \tag{3.10}$$

Similarly, we derive

$$\frac{\partial}{\partial t}(s_k k|u^{s_k}|^2 + s_p p|u^{s_p}|^2 + s_q q|u^{s_q}|^2) = -2\nu(s_k k^3|u^{s_k}|^2 + s_p p^3|u^{s_p}|^2 + s_q q^3|u^{s_q}|^2) \tag{3.11}$$

from (3.7). In (3.10) and (3.11), the wavenumber vectors satisfy $\boldsymbol{k} + \boldsymbol{p} + \boldsymbol{q} = \boldsymbol{0}$, and the summation convention over repeated indices s_k, s_p and s_q is not applied.

Letting $\boldsymbol{p} = -\boldsymbol{k}$ and $\boldsymbol{q} = \boldsymbol{0}$ in (3.11) and summing over $\boldsymbol{k}$ yields

$$\frac{\mathrm{d}\mathcal{H}}{\mathrm{d}t} = -2\nu L^3\sum_{\boldsymbol{k}} k^3(|u^+(\boldsymbol{k}, t)|^2 - |u^-(\boldsymbol{k}, t)|^2). \tag{3.12}$$

This equation, similar to (2.29) in Chen *et al.* (2003*a*), divides the velocity components altering $\mathcal{H}$ in terms of the chirality and scale, so that we can pinpoint which part causes a notable variation to $\mathcal{H}$.

Considering flows at very high Reynolds numbers with $\nu \ll 1$, $L = O(1)$ and $|u^{\pm}(\boldsymbol{k}, t)|^2 \leq O(1)$, the contribution from small k in (3.12) can be ignored due to the weight k^3. Thus, we define a truncated wavenumber

$$k_c \equiv \mathcal{U}^{1/3}\mathcal{L}^{-2/3}\nu^{-1/3}, \tag{3.13}$$

to demarcate the energy-containing and inertial ranges, and a characteristic wavenumber (Pope 2000)

$$k_{\mathrm{DI}} \equiv \mathcal{U}^{3/4}\mathcal{L}^{-1/4}\nu^{-3/4} > k_c, \tag{3.14}$$

to demarcate the inertial and dissipative ranges, with characteristic velocity $\mathcal{U}$ and length scale $\mathcal{L}$. In general, the major contribution to $\mathrm{d}\mathcal{H}/\mathrm{d}t$ comes from small-scale structures as

$$\frac{\mathrm{d}\mathcal{H}}{\mathrm{d}t} \approx -2\nu L^3 \sum_{k>k_c} k^3(|u^+(\boldsymbol{k},t)|^2 - |u^-(\boldsymbol{k},t)|^2). \tag{3.15}$$

By contrast, the total helicity is determined by large-scale structures. Applying the model helicity spectra with power-law and exponential decay to moderate and high wavenumbers (Brissaud *et al.* 1973; Ditlevsen & Giuliani 2001), respectively, we estimate

$$\begin{aligned}\left|\sum_{k>k_c} k(|u^+(\boldsymbol{k},t)|^2 - |u^-(\boldsymbol{k},t)|^2)\right| &\le \left|\sum_{k_c<k<k_{\mathrm{DI}}} C_{\mathcal{H}} k^{-n}\right| + \left|\sum_{k\ge k_{\mathrm{DI}}} k\,\mathrm{e}^{-\beta k}(C^+ - C^-)\right| \\ &\le C_1(k_{\mathrm{DI}}^{1-n} - k_c^{1-n}) + C_2\frac{1+\beta k_{\mathrm{DI}}}{\beta^2}\,\mathrm{e}^{-\beta k_{\mathrm{DI}}} \\ &= -C_3\nu^{(n-1)/3} + O(\nu^{3(n-1)/4}),\end{aligned} \tag{3.16}$$

with model parameters $C_{\mathcal{H}}$, C^+ and C^-, and constants

$$\left.\begin{aligned} C_1 &= \frac{1}{1-n}\max_{k_c<k<k_{\mathrm{DI}}}\{|C_{\mathcal{H}}|\}, \\ C_2 &= \max_{k\ge k_{\mathrm{DI}}}\{|C^+ - C^-|\}, \\ C_3 &= C_1\mathcal{U}^{(1-n)/3}\mathcal{L}^{-2(1-n)/3}, \end{aligned}\right\} \tag{3.17}$$

and $4/3 \le n \le 5/3$. For $n > 1$, (3.16) is a high-order small term, so $\mathcal{H}(t)$ is mainly contributed from scales larger than $2\pi/k_c$ as

$$\mathcal{H}(t) = L^3 \sum_{k\le k_c} k(|u^+(\boldsymbol{k},t)|^2 - |u^-(\boldsymbol{k},t)|^2) + O(\nu^{(n-1)/3}). \tag{3.18}$$

We define

$$\mathcal{H}^{\pm}_{<}(t) \equiv L^3 \sum_{k\le k_c} k|u^{\pm}|^2 \quad \text{and} \quad \mathcal{H}^{\pm}_{>}(t) \equiv L^3 \sum_{k>k_c} k|u^{\pm}|^2 \tag{3.19a,b}$$

for large and small scales, respectively. Then, (3.18) is re-expressed as

$$\mathcal{H}(t) \approx \mathcal{H}^+_{<}(t) - \mathcal{H}^-_{<}(t). \tag{3.20}$$

From (3.15) and (3.20), we derive

$$\left.\begin{aligned} \frac{\mathrm{d}\mathcal{H}}{\mathrm{d}t} &> 0, \quad \text{if } \mathcal{H}^+_{>} < \mathcal{H}^-_{>}, \\ \frac{\mathrm{d}\mathcal{H}}{\mathrm{d}t} &< 0, \quad \text{if } \mathcal{H}^+_{>} > \mathcal{H}^-_{>}. \end{aligned}\right\} \tag{3.21}$$

Here, the difference between the left- and right-handed components of the small-scale helicity needs to satisfy

$$\left|\sum_{k>k_c} k^3(|u^+(\boldsymbol{k},t)|^2 - |u^-(\boldsymbol{k},t)|^2)\right| \gg \left|\sum_{k\le k_c} k^3(|u^+(\boldsymbol{k},t)|^2 - |u^-(\boldsymbol{k},t)|^2)\right|, \tag{3.22}$$

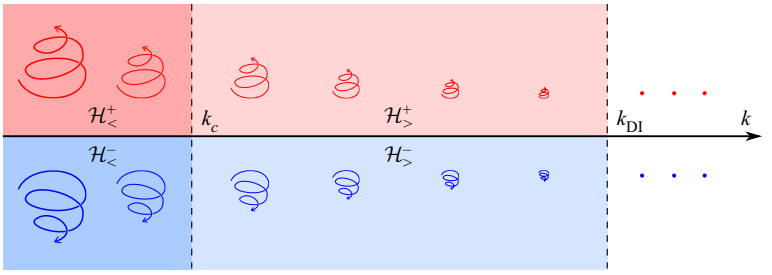

Figure 1. Schematic diagram for the influence of small-scale chiral helicity components on large-scale components in Fourier space at large Re. The superscripts '+' and '−' denote the right-handed (red in upper row) and left-handed (blue in lower row) components, respectively. The wavenumbers are plotted in a logarithmic scale, and characteristic wavenumbers are marked by dashed lines.

which requires

$$|\mathcal{H}^+_> - \mathcal{H}^-_>| \gg k_c^{-2} O(k_c) = O(\nu^{1/3}) \tag{3.23}$$

in (3.21).

As illustrated in figure 1, (3.21) indicates that small-scale left-handed (or right-handed) structures can drive the generation of large-scale right-handed (or left-handed) structures, leading to the time variation of $\mathcal{H}$. This explains the 'transient growth' of $\mathcal{H}$ during the reconnection of a trefoil knot, in which Yao *et al.* (2021) observed that $\mathcal{H}^-_>$ is slightly larger than $\mathcal{H}^+_>$. Therefore, the breaking of parity symmetry at small scales can strongly alter the total helicity, which is further discussed in Appendix A.

3.3. *Pentadic interactions in the HCNS dynamics*

We investigate the HCNS dynamics in Fourier space based on the HWD. Substituting (3.1), (3.3) and the HWD of the squared vorticity magnitude

$$|\boldsymbol{\omega}|^2 = \sum_{\boldsymbol{p},\boldsymbol{q}} pq(u_p^+ \boldsymbol{h}_p^+ - u_p^- \boldsymbol{h}_p^-) \cdot (u_q^+ \boldsymbol{h}_q^+ - u_q^- \boldsymbol{h}_q^-)\, \mathrm{e}^{\mathrm{i}(\boldsymbol{p}+\boldsymbol{q})\cdot\boldsymbol{x}} \tag{3.24}$$

into the HCNS equation (2.10), we derive

$$\begin{aligned} &mn(u_m^+ \boldsymbol{h}_m^+ - u_m^- \boldsymbol{h}_m^-) \cdot (u_n^+ \boldsymbol{h}_n^+ - u_n^- \boldsymbol{h}_n^-)[(\partial_t + \nu k^2)(u_k^+ \boldsymbol{h}_k^+ + u_k^- \boldsymbol{h}_k^-) + \mathrm{i}\hat{P}_k \boldsymbol{k}] \\ &\quad - \nu mnk^2 (u_m^+ \boldsymbol{h}_m^+ - u_m^- \boldsymbol{h}_m^-) \cdot (u_k^+ \boldsymbol{h}_k^+ + u_k^- \boldsymbol{h}_k^-)(u_n^+ \boldsymbol{h}_n^+ - u_n^- \boldsymbol{h}_n^-) \\ &\quad + \sum_{\boldsymbol{p}+\boldsymbol{q}+\boldsymbol{r}+\boldsymbol{s}=\boldsymbol{k}+\boldsymbol{m}+\boldsymbol{n}} prs[(u_p^+ \boldsymbol{h}_p^+ - u_p^- \boldsymbol{h}_p^-) \times (u_q^+ \boldsymbol{h}_q^+ + u_q^- \boldsymbol{h}_q^-)] \\ &\quad \times [(u_r^+ \boldsymbol{h}_r^+ - u_r^- \boldsymbol{h}_r^-) \cdot (u_s^+ \boldsymbol{h}_s^+ - u_s^- \boldsymbol{h}_s^-)] \\ &= 0, \end{aligned} \tag{3.25}$$

where $\boldsymbol{k}$, $\boldsymbol{m}$ and $\boldsymbol{n}$ are not restrained from each other, and the subscript denotes the corresponding wavenumber vector, e.g. $\boldsymbol{h}_k$ is a shorthand for $\boldsymbol{h}(\boldsymbol{k}, t)$. Letting $\boldsymbol{m} = \boldsymbol{k}$ and

$\boldsymbol{n} = -\boldsymbol{k}$, we obtain

$$\begin{aligned} &2k^2E_k(\partial_t + \nu k^2)u_k^{\pm} \\ &\quad = -\sum_{\boldsymbol{p}+\boldsymbol{q}+\boldsymbol{r}+\boldsymbol{s}=\boldsymbol{k}} prs[\boldsymbol{h}_k^{\mp}\cdot(u_p^+\boldsymbol{h}_p^+ - u_p^-\boldsymbol{h}_p^-)\times(u_q^+\boldsymbol{h}_q^+ + u_q^-\boldsymbol{h}_q^-)] \\ &\qquad \times[(u_r^+\boldsymbol{h}_r^+ - u_r^-\boldsymbol{h}_r^-)\cdot(u_s^+\boldsymbol{h}_s^+ - u_s^-\boldsymbol{h}_s^-)], \end{aligned} \tag{3.26}$$

with $E_k = (|u_k^+|^2 + |u_k^-|^2)/2$ after some algebra. It can be further written in a more symmetric and compact form as

$$\begin{aligned} &4k^2E_k(\partial_t + \nu k^2)u^{s_k*} \\ &\quad = -\sum_{\boldsymbol{k}+\boldsymbol{p}+\boldsymbol{q}+\boldsymbol{r}+\boldsymbol{s}=\boldsymbol{0}}\ \sum_{s_p,s_q,s_r,s_s} (s_pp - s_qq)s_rs_srs(\boldsymbol{h}^{s_k}\cdot\boldsymbol{h}^{s_p}\times\boldsymbol{h}^{s_q})(\boldsymbol{h}^{s_r}\cdot\boldsymbol{h}^{s_s})u^{s_p}u^{s_q}u^{s_r}u^{s_s}. \end{aligned} \tag{3.27}$$

In (3.27), the mode interaction in Fourier space takes place among pentads of wavenumbers with $\boldsymbol{k}+\boldsymbol{p}+\boldsymbol{q}+\boldsymbol{r}+\boldsymbol{s}=\boldsymbol{0}$. There are 32 interaction types with $(s_k, s_p, s_q, s_r, s_s) = (\pm,\pm,\pm,\pm,\pm)$, and 16 of them are independent. Therefore, the pentadic interactions in the HCNS dynamics are more complex than the triadic interactions in the NS dynamics, due to the imposed helicity conservation on a viscous flow.

Similar to the derivation for the NS flow, we obtain

$$\begin{aligned} &(\partial_t + 2\nu k^2)|u^{s_k}|^2 \\ &\quad = -\frac{1}{4k^2E_k}\sum_{\boldsymbol{k}+\boldsymbol{p}+\boldsymbol{q}+\boldsymbol{r}+\boldsymbol{s}=\boldsymbol{0}}\ \sum_{s_p,s_q,s_r,s_s} \mathcal{T}(\boldsymbol{k},\boldsymbol{p},\boldsymbol{q})\mathcal{T}'(\boldsymbol{r},\boldsymbol{s})u^{s_k}u^{s_p}u^{s_q}u^{s_r}u^{s_s} + \text{c.c.}, \end{aligned} \tag{3.28}$$

with

$$\mathcal{T}'(\boldsymbol{r},\boldsymbol{s}) = s_rs_srs(\boldsymbol{h}^{s_r}\cdot\boldsymbol{h}^{s_s}). \tag{3.29}$$

From (3.8) and (3.28), we derive the evolution equations of the left- and right-handed helicity components for the NS/HCNS flow as

$$\frac{\mathrm{d}\mathcal{H}^{s_k}_{\mathrm{NS/HCNS}}}{\mathrm{d}t} = -\mathcal{E}^{s_k} + \mathcal{P}^{s_k}_{\mathrm{NS/HCNS}}, \tag{3.30}$$

with

$$\mathcal{E}^{s_k} = 2\nu L^3\sum_{\boldsymbol{k}} k^3|u^{s_k}|^2, \tag{3.31}$$

$$\mathcal{P}^{s_k}_{\mathrm{NS}} = -\frac{L^3}{2}\sum_{\boldsymbol{k}} k\sum_{\boldsymbol{k}+\boldsymbol{p}+\boldsymbol{q}=\boldsymbol{0}}\ \sum_{s_p,s_q}\mathcal{T}(\boldsymbol{k},\boldsymbol{p},\boldsymbol{q})u^{s_k}u^{s_p}u^{s_q} + \text{c.c.}, \tag{3.32}$$

$$\mathcal{P}^{s_k}_{\mathrm{HCNS}} = -\frac{L^3}{2}\sum_{\boldsymbol{k}} k\sum_{\boldsymbol{k}+\boldsymbol{p}+\boldsymbol{q}+\boldsymbol{r}+\boldsymbol{s}=\boldsymbol{0}}\ \sum_{s_p,s_q}\mathcal{S}(\boldsymbol{k},\boldsymbol{r},\boldsymbol{s})\mathcal{T}(\boldsymbol{k},\boldsymbol{p},\boldsymbol{q})u^{s_k}u^{s_p}u^{s_q} + \text{c.c.}, \tag{3.33}$$

and a stretch factor

$$\mathcal{S}(\boldsymbol{k},\boldsymbol{r},\boldsymbol{s}) = \frac{1}{2k^2E_k}\sum_{s_r,s_s}\mathcal{T}'(\boldsymbol{r},\boldsymbol{s})u^{s_r}u^{s_s} = \frac{1}{2}\sum_{s_r,s_s}s_rs_s\frac{rs}{k^2}\frac{u^{s_r}u^{s_s}}{E_k}(\boldsymbol{h}^{s_r}\cdot\boldsymbol{h}^{s_s}). \tag{3.34}$$

Since the convective term dominates flow dynamics at large Re, we assume that the major part of the pentadic interactions in the HCNS dynamics are still the triadic

interactions. Thus, (3.33) becomes

$$\mathcal{P}^{s_k}_{\mathrm{HCNS}} = \left(-\frac{L^3}{2} \sum_{\boldsymbol{k}} k \sum_{\boldsymbol{k}+\boldsymbol{p}+\boldsymbol{q}=\boldsymbol{0}} \sum_{\boldsymbol{r}+\boldsymbol{s}=\boldsymbol{0}} \sum_{s_p,s_q} \mathcal{S}(\boldsymbol{k},\boldsymbol{r},\boldsymbol{s})\mathcal{T}(\boldsymbol{k},\boldsymbol{p},\boldsymbol{q}) u^{s_k} u^{s_p} u^{s_q} + \mathrm{c.c.} \right) + \mathrm{h.o.t.}, \tag{3.35}$$

where h.o.t. denotes a higher-order term. From the orthogonality of $\boldsymbol{h}^{\pm}$, we find

$$\begin{aligned} \sum_{\boldsymbol{r}+\boldsymbol{s}=\boldsymbol{0}} \mathcal{S}(\boldsymbol{k},\boldsymbol{r},\boldsymbol{s}) &= \frac{1}{2} \sum_{\boldsymbol{r}} \sum_{s_r,s_s} s_r s_s \frac{r^2}{k^2} \frac{u^{s_r}(\boldsymbol{r}) u^{s_s *}(\boldsymbol{r})}{E_k} (\boldsymbol{h}^{s_r}(\boldsymbol{r}) \cdot \boldsymbol{h}^{s_s *}(\boldsymbol{r})) \\ &= \frac{1}{2k^2 E_k} \sum_{\boldsymbol{r}} r^2 (u^+(\boldsymbol{r}) u^{+*}(\boldsymbol{r}) + u^-(\boldsymbol{r}) u^{-*}(\boldsymbol{r})) \\ &= \frac{1}{k^2 E_k} \sum_{\boldsymbol{r}} r^2 E_r > 1. \end{aligned} \tag{3.36}$$

Comparing (3.32) and (3.35) with (3.36) yields $|\mathcal{P}^{s_k}_{\mathrm{HCNS}}| > |\mathcal{P}^{s_k}_{\mathrm{NS}}|$. Integrating (3.30) yields

$$\mathcal{H}^{s_k}_{\mathrm{NS/HCNS}} = \mathcal{H}^{s_k}_0 - \int_0^t \mathcal{E}^{s_k} \,\mathrm{d}t' + \int_0^t \mathcal{P}^{s_k}_{\mathrm{NS/HCNS}} \,\mathrm{d}t'. \tag{3.37}$$

Considering the production $\mathcal{P}^{s_k} > 0$ in general, we obtain

$$\mathcal{H}^{\pm}_{\mathrm{HCNS}} > \mathcal{H}^{\pm}_{\mathrm{NS}}. \tag{3.38}$$

Starting from the same initial condition, (3.38) indicates that the left- or right-handed helicity component in the HCNS flow is larger than its counterpart in the NS flow.

4. Simulation overview

The DNS is performed to solve (2.1) and (2.4) with $\boldsymbol{F} = \nu\nabla^2\boldsymbol{u}$ for the NS flow and $\boldsymbol{F} = \nu(\boldsymbol{n}_\omega \times \nabla^2\boldsymbol{u}) \times \boldsymbol{n}_\omega$ for the HCNS flow. It is carried out using the pseudo-spectral method in a periodic cube of side $L = 2\pi$ on N^3 uniform grid points. Aliasing errors are removed using the two-thirds truncation method with the maximum wavenumber $k_{\max} \approx N/3$.

Note that strictly speaking the $N/5$ dealiasing rule should be used in the presence of the fifth-order nonlinear interaction for the HCNS equation. Consistent with the conjectured dominance of triadic interactions in (3.35), we found that the $N/3$ rule is still sufficient in numerical tests. The temporal evolution is integrated using an explicit second-order Runge–Kutta scheme with adaptive time steps in physical space. The spatial resolution, i.e. N, is selected to resolve the smallest motion by grid convergence tests as in Yao *et al.* (2021). The time step Δt is selected to ensure that the Courant–Friedrichs–Lewy number small enough (0.1–0.3 for different cases) for numerical stability and accuracy. We set up several DNS cases with $Re = 1/\nu$ and different initial conditions. The DNS parameters are listed in table 1.

There are two types of initial conditions. For the first type, the initial vorticity is concentrated in a thin closed vortex tube, such as the vortex ring and vortex knot. The parametric equation of the tube centreline $\mathcal{C}$, a spatially closed curve, is

$$\boldsymbol{c}(\zeta) = [R_0 + r_0\cos(q\zeta)]\cos(p\zeta)\boldsymbol{e}_x + [R_0 + r_0\cos(q\zeta)]\sin(p\zeta)\boldsymbol{e}_y - [r_0\sin(q\zeta) + 2]\boldsymbol{e}_z, \tag{4.1}$$

with $\zeta \in [0, 2\pi)$ and unit vectors $\{\boldsymbol{e}_x, \boldsymbol{e}_y, \boldsymbol{e}_z\}$ for Cartesian coordinates. Geometric/topological parameters W_{r0}, T_{w0}, R_0, r_0, p and q for different cases are listed in table 1.

Cases	Re	N^3	$\mathcal{H}_0$	W_{r0}	T_{w0}	Γ	R_0	r_0	(p, q)
Twisted ring	1000	512^3	10	0	10	1	1	0	(1, 1)
Trefoil knot	2000	1024^3	3.518	3.518	0	1	1	0.5	(2, 3)
Colliding rings	2000	1024^3	0	0	0	1	1	0	(1, 1)
HIT	500	512^3	−104.5	—	—	—	—	—	—

Table 1. DNS cases and parameters.

Here, the writhe W_r characterizes the degree of distortion of $\mathcal{C}$ and T_w characterizes the twist of a ribbon formed by $\mathcal{C}$ and its accompanying curve. Their definitions and geometric meanings are detailed in Moffatt & Ricca (1992). For a closed vortex tube with uniform twist, the total helicity has the decomposition $\mathcal{H} = \Gamma^2(W_r + T_w)$, where Γ is the circulation of the vortex tube.

We use the method adapted from Xiong & Yang (2019*a*, 2020) to construct unknotted or knotted vortex tubes with finite thickness and tunable twist. The case set-ups are very similar to those in Xiong & Yang (2020) and Yao *et al.* (2021), so they are only briefly discussed below. The vorticity flux distribution is a Gaussian function with $\Gamma = 1$ and standard deviation $\sigma_0 = 1/(16\sqrt{2\pi}) \approx 0.025$. The effective core radius is estimated as $r_e = 2\sigma_0$, within which the vortex tube contains 95 % of the circulation. The vortex tube is sufficiently thin corresponding to the criterion in Zhao *et al.* (2021). The velocity field is calculated by the Biot–Savart law $\boldsymbol{u}(\boldsymbol{x}) = \mathcal{F}^{-1}(\mathrm{i}\boldsymbol{k} \times \hat{\boldsymbol{\omega}}/k^2)$ in Fourier space, where $\hat{\boldsymbol{\omega}} = \mathcal{F}(\boldsymbol{\omega})$ denotes the Fourier coefficient of the vorticity field with the Fourier transform operator $\mathcal{F}$ and its inverse form $\mathcal{F}^{-1}$.

For the second type of initial condition, the initial velocity $\boldsymbol{u}_0$ is a Gaussian random field for simulating decaying HIT (Xiong & Yang 2019*b*), with volume-averaged initial energy $\langle E_0 \rangle = E_0/L^3 = 1$ and a prescribed energy spectrum (Kraichnan 1970; Ishida, Davidson & Kaneda 2006; Briard & Gomez 2017) $E_k(k, t = 0) \sim k^4 \exp[-2(k/4)^2]$.

5. Evolution of HCNS flows

For the cases of the twisted vortex ring, trefoil vortex knot and colliding vortex rings in table 1, the NS flows show significant changes of $\mathcal{H}$ with essential vortex dynamics, such as vorticity diffusion and vortex reconnection. For the case of HIT, the NS flow has decaying $\mathcal{H}$ and energy cascade with time. We demonstrate how the imposed helicity conservation changes vortex and helicity dynamics in HCNS flows, and its implication to parity breaking in NS flows.

5.1. *Twisted ring*

We investigate a vortex ring with an initially uniform twist with $W_r = 0$ and $T_{w0} = 10$. This is a simple model for the decay of $\mathcal{H}$ or T_w in NS flows. Figure 2 depicts the temporal evolution of the isosurface of $|\boldsymbol{\omega}|$ in HCNS and NS flows. Here, the time t can be considered as a normalized one: $t/(R_0^2/\Gamma)$ with $R_0^2/\Gamma = 1$. In the NS flow, the helical degree of vortex lines, characterized by T_w, diminishes with time. By contrast, the ring shape and helical vortex lines are maintained in the HCNS flow due to the imposed helicity conservation. Figure 3(*b*) shows the persistent growth of Λ_B, i.e. the Beltramization of the HCNS flow analysed in § 2.3, which is distinguished from the decaying Λ_B in the NS flow.

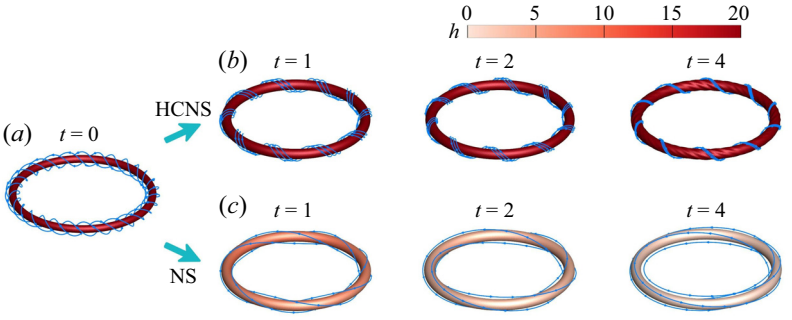

Figure 2. Evolution of the isosurface of $|\boldsymbol{\omega}|$ for (*a*) the twisted vortex ring in (*b*) HCNS and (*c*) NS flows. The isocontour thresholds are $|\boldsymbol{\omega}| = 25, 25, 25, 20$ for the HCNS flow and $|\boldsymbol{\omega}| = 25, 20, 17, 13$ for the NS flow at $t = 0, 1, 2, 4$, respectively. The isosurfaces are colour-coded by the helicity density.

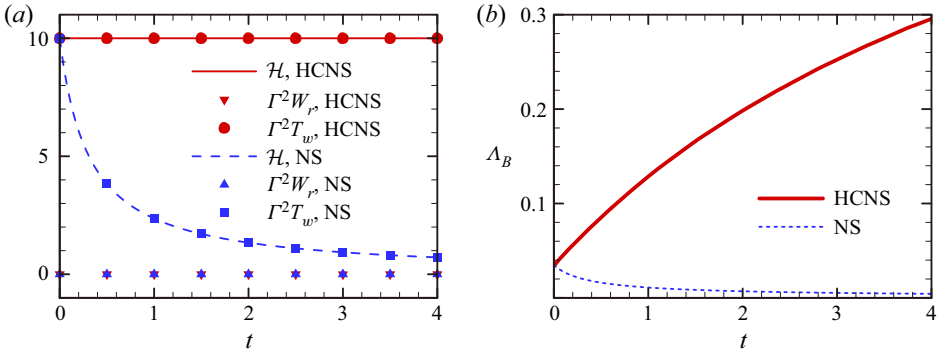

Figure 3. Evolution of (*a*) the helicity and its components and (*b*) the Beltramization criterion for the twisted vortex ring in HCNS and NS flows.

At long times, $\boldsymbol{u}$ and $\boldsymbol{\omega}$ tend to be aligned to maintain $\mathcal{H}$ with decaying $|\boldsymbol{u}|$ and $|\boldsymbol{\omega}|$ in the HCNS flow.

The large-scale ring structures in both flows are the same. In figure 3(*a*), both vortex centrelines keep as a circle with $W_r = 0$, where W_r is calculated by the method in Yao *et al.* (2021). Thus, the helicity variation in the NS flow is totally due to the decay of T_w in figure 3(*a*), whereas T_w is conserved in the HCNS flow. Note that the local twist within the vortex ring can be non-uniform in the HCNS flow.

In figure 4, the total energy of the HCNS flow persistently decays with time, and the decaying of E and Ω in the HCNS flow is slower than that in the NS flow, consistent with (2.18) and (2.25).

5.2. *Trefoil knot*

We investigate the evolution of a trefoil knotted vortex tube with $W_r > 0$ and $T_{w0} = 0$ to show how the imposed helicity conservation influences the vortex reconnection, which plays an essential role in the dynamics of viscous flows (Kida & Takaoka 1994; Yao & Hussain 2022). Moreover, we examine the theory in § 3.2 that the breaking of parity symmetry at small scales leads to a sudden change of $\mathcal{H}$ during vortex reconnection.

In figure 5, the evolutions of large-scale vortical structures in NS and HCNS flows are very similar. Driven by the self-induced velocity, the knotted vortex tube is untied into a

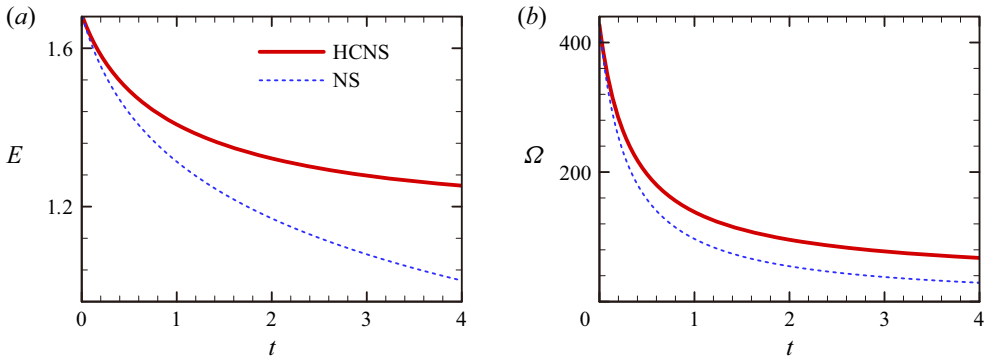

Figure 4. Evolution of (*a*) total kinetic energy and (*b*) enstrophy for the twisted vortex ring in HCNS and NS flows.

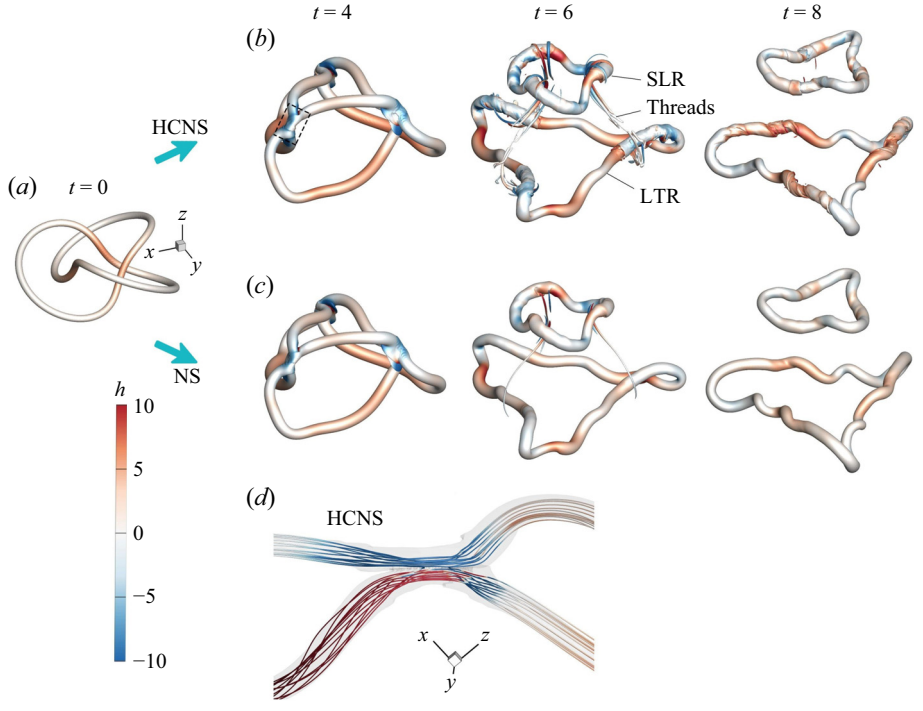

Figure 5. Evolution of the isosurface of $|\boldsymbol{\omega}| = 0.04\omega_0$ for (*a*) the trefoil knot in (*b*) HCNS and (*c*) NS flows, with $\omega_0 = |\boldsymbol{\omega}_0|_{max}$, the maximum value of $|\boldsymbol{\omega}_0|$ in the computational domain. The SLR, LTR and threads are marked. (*d*) Close-up view of vortex lines at the reconnection site at $t = 4$ in the HCNS flow, and the region is marked by the dashed box in (*b*). All isosurfaces and vortex lines are colour-coded by the helicity density.

large tailing ring (LTR) and a small leading ring (SLR) via vortex reconnection. Strong positive and negative helicity density are generated locally near reconnection sites. The close-up view of the reconnection region in figure 5(*d*) shows that the vortex lines are not strictly anti-parallel in the HCNS flow, and their geometry in the NS flow is very similar, so the writhe and twist can vary during the reconnection with helicity conservation (Laing, Ricca & Sumners de 2015).

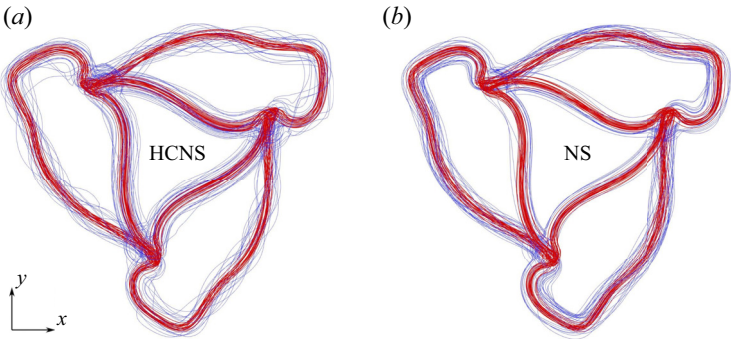

Figure 6. Top view of vortex lines for the trefoil knot at $t = 4$ when the vortex reconnection occurs in (a) HCNS and (b) NS flows. Red and blue vortex lines are integrated from points on the isosurface of $|\boldsymbol{\omega}| = 0.16\omega_0$ and $|\boldsymbol{\omega}| = 0.04\omega_0$, respectively.

For further quantitative comparisons (not shown), the total length and writhe of the vortex core line, which were reported in figures 6 and 10 in Yao *et al.* (2021), are very close in NS and HCNS flows, and the generalized twist $\mathcal{H}/\Gamma^2 - W_r$ in the HCNS flow is slightly larger than in the NS flow. The total helicity remains conserved in the HCNS flow, while it fluctuates during vortex reconnection (Yao *et al.* 2021). Therefore, although the helicity characterizes the flow topology, vortex reconnection in the HCNS flow indicates that the helicity can be invariant during significant topological changes of vortex lines or tubes by altering internal structures within vortex tubes.

The evolution of the vortex knot in NS flows shows a significant variation of $\mathcal{H}$ and even a transient growth at large Re (Yao *et al.* 2021; Zhao & Scalo 2021; Zhao *et al.* 2021). On the contrary, the HCNS flow conserves the helicity by maintaining or generating a larger twist than that in the NS flow. Figure 6 shows the vortex lines within the vortex tube in HCNS and NS flows at the reconnection time. The vortex lines near the vortex core remain parallel in both flows, and they become chaotic and non-uniform in the outer tube in the HCNS flow. Then the trefoil knot is split into the LTR and SLR, and the chaotic vortex lines in the HCNS flow show strong non-uniform twist in figure 5(b), corresponding to the Beltramization of the HCNS flow.

Figure 7(a) shows that both left- and right-handed helicity components in the HCNS flow are larger than their counterparts in the NS flow, consistent with the stronger twist in figure 6 and the theoretical analysis in (3.38). Figure 7(b) shows that the HCNS energy spectrum is larger than the NS one at late times in the dissipation range, as a quantification for the more small-scale structures in the HCNS flow in figures 5 and 6. Moreover, $E_k(k)$ shows a k^{-4} law in the dissipation range in the HCNS flow, and it remains in the evolution at late times.

We explain the transient variation of $\mathcal{H}$ (see figure 8) during the vortex reconnection of the trefoil knot in the NS flow using the HWD analysis in § 3.2. For simple closed vortex tubes such as knots or links, we take the characteristic length $\mathcal{L} = R_0$ and velocity $\mathcal{U} = \Gamma/\sigma(t)$, where the growth of the vortex core size σ due to the viscous diffusion is estimated by $\sigma(t) = \sqrt{\sigma_0^2 + 2\nu t}$ from the Lamb–Oseen vortex model (Wu, Ma & Zhou 2015). The truncated wavenumber in (3.13) becomes

$$k_c(t) = \Gamma^{1/3} R_0^{-2/3} \nu^{-1/3} (\sigma_0^2 + 2\nu t)^{-1/6}, \tag{5.1}$$

which initially is $k_c(0) \approx 43.1$ at $Re = 2000$ and decreases with increasing time. Then, we use the HWD to calculate $\mathcal{H}_<^{\pm}$ and $\mathcal{H}_>^{\pm}$ by (3.19a,b).

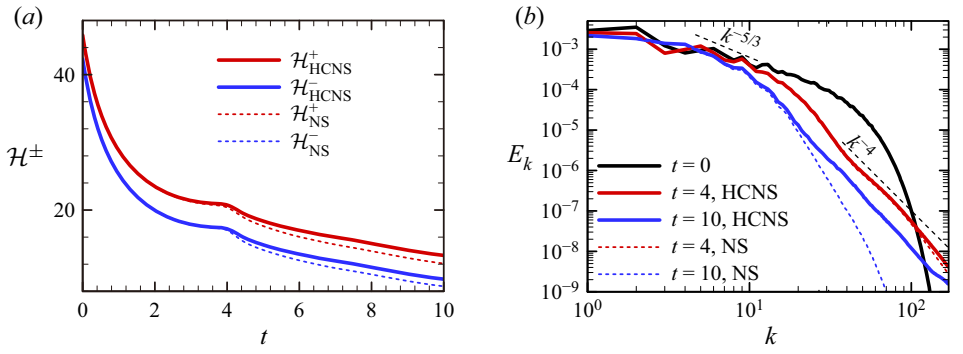

Figure 7. (*a*) Evolution of the left- and right-handed helicity components and (*b*) energy spectra at $t = 0$, 4 and 10 for the trefoil vortex knot in HCNS and NS flows.

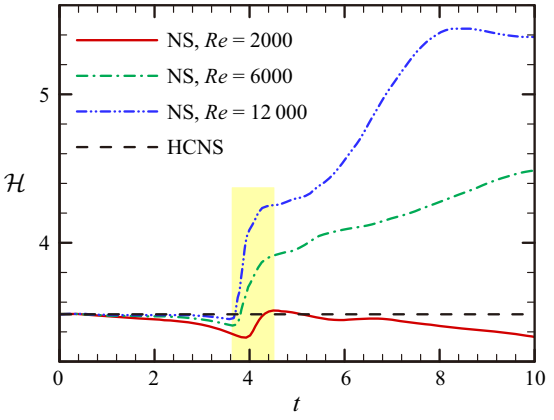

Figure 8. Evolution of helicity for the trefoil knot in HCNS and NS flows. The profiles for the NS flow at $Re = 6000$ and 12 000 are adapted from Yao *et al.* (2021). The time period of the transient growth of $\mathcal{H}$ during vortex reconnection is shaded in yellow.

In figure 9(*a*), the notable difference of the left- and right-handed helicity spectra

$$\mathcal{H}^{\pm}_{k}(k) \equiv \sum_{k'} k' |u^{\pm}(\boldsymbol{k}')|^2 \delta(|\boldsymbol{k}'| - k) \tag{5.2}$$

at $k > k_c$ (shaded in yellow) indicates that parity breaking at small scales occurs during vortex reconnection in the NS flow, where k_c is marked by the vertical dashed line. In figure 9(*b*) around $t = 4$ (shaded in yellow), finite $\mathcal{H}^{-}_{>} - \mathcal{H}^{+}_{>}$ appears to cause a spike of $\mathrm{d}\mathcal{H}/\mathrm{d}t$, because the peak of $\mathcal{H}^{-}_{>} - \mathcal{H}^{+}_{>}$ occurs slightly earlier than the peak of $\mathrm{d}\mathcal{H}/\mathrm{d}t$. The causality of the transient variation of $\mathcal{H}$ and small-scale parity breaking is further discussed in Appendix A. An overall agreement of the peaks of $\mathrm{d}\mathcal{H}/\mathrm{d}t$ and the right-hand side of (3.15) shows that the helicity variation is dominated by small-scale motions. Since parity breaking at small scales seems to be unavoidable in practical flows under various disturbances and instabilities, helicity conservation cannot be ensured, perhaps even in the inviscid limit, in the NS flow.

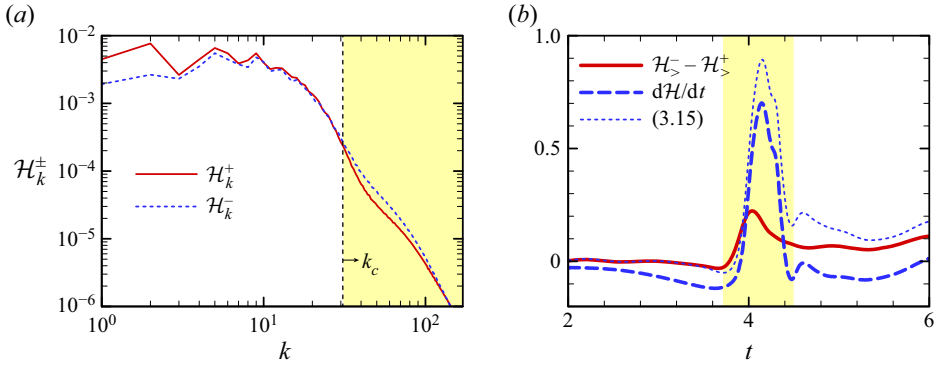

Figure 9. Parity breaking at small scales in the evolution of the trefoil vortex knot in the NS flow at $Re = 2000$. (*a*) Left- and right-handed helicity spectra at $t = 4$. (*b*) Evolution of the difference between left- and right-handed helicity components at small scales, the time rate of helicity and right-hand side of (3.15).

5.3. *Asymmetric collision of vortex rings*

We study the helicity dynamics of the asymmetric collision of vortex rings (Yao *et al.* 2022) with $\mathcal{H}_0 = 0$ in NS and HCNS flows. The parametric equations of the vortex centrelines of two initial unlinked vortex rings are

$$\boldsymbol{c}_1(\zeta) = \left[\frac{\sqrt{2}}{2}(\cos\zeta + \sin\theta\sin\zeta) - \delta\right]\boldsymbol{e}_x - \cos\theta\sin\zeta\,\boldsymbol{e}_y + \frac{\sqrt{2}}{2}(\cos\zeta - \sin\theta\sin\zeta)\boldsymbol{e}_z \tag{5.3}$$

and

$$\boldsymbol{c}_2(\zeta) = \left(\frac{\sqrt{2}}{2}\cos\zeta - \delta\right)\boldsymbol{e}_x - \sin\zeta\,\boldsymbol{e}_y - \frac{\sqrt{2}}{2}\cos\zeta\,\boldsymbol{e}_z. \tag{5.4}$$

Here, $\theta = \pi/8$ is a rotating angle to pose asymmetry and $\delta = 0.85$ is a separation distance. Other initial parameters of the two rings, $R_0 = 1$, $\Gamma = 1$ and $\sigma_0 = 1/(16\sqrt{2\pi})$, are the same as those for the trefoil knot. The initial configuration is shown in figure 11(*a*).

Starting from $\mathcal{H} = 0$, the helicity in the NS flow fluctuates in figure 10(*a*) due to the asymmetric vortex reconnection in figure 11. Similar to the observation for the trefoil vortex knot, large-scale structures in NS and HCNS flows are almost identical in figure 11, while small-scale ones show notable differences. In figure 11(*e*), the small-scale threads in the NS flow show that the positive helicity density is stronger than the negative one, leading to $\mathcal{H} > 0$. By contrast, the HCNS flow generates numerous small-scale structures in figures 11(*a*) and 11(*d*) at $t = 2$, much more than in the NS flow. The extra threads make a delicate balance of $\mathcal{H}^+$ and $\mathcal{H}^-$. In § 3.3, we demonstrate that the pentadic interactions in the HCNS dynamics are more complex than the triadic interactions in the NS dynamics. Figure 10 shows $\mathcal{H}^{\pm}_{\mathrm{HCNS}}$ is slightly larger than $\mathcal{H}^{\pm}_{\mathrm{NS}}$, consistent with (3.38).

The asymmetric collision of vortex rings also shows that parity breaking at small scales leads to helicity variation in the NS flow. As analysed in § 3.2 and shown in figure 12, all peaks or valleys of $\mathcal{H}_>^- - \mathcal{H}_>^+$ are slightly ahead of those of $\mathrm{d}\mathcal{H}/\mathrm{d}t$, and the profiles of $\mathrm{d}\mathcal{H}/\mathrm{d}t$ and the right-hand side of (3.15) almost collapse, where k_c in (5.1) is used. For comparison, helicity conservation in the HCNS flow with $\mathcal{H}_0 = 0$ implies absolute parity symmetry through the pentadic mode interactions.

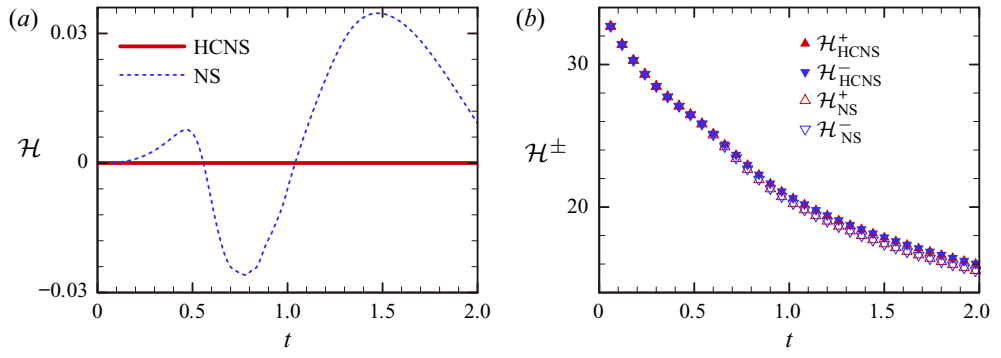

Figure 10. Evolution of (*a*) helicity and (*b*) left- and right-handed helicity components for the asymmetric collision of vortex rings in HCNS and NS flows.

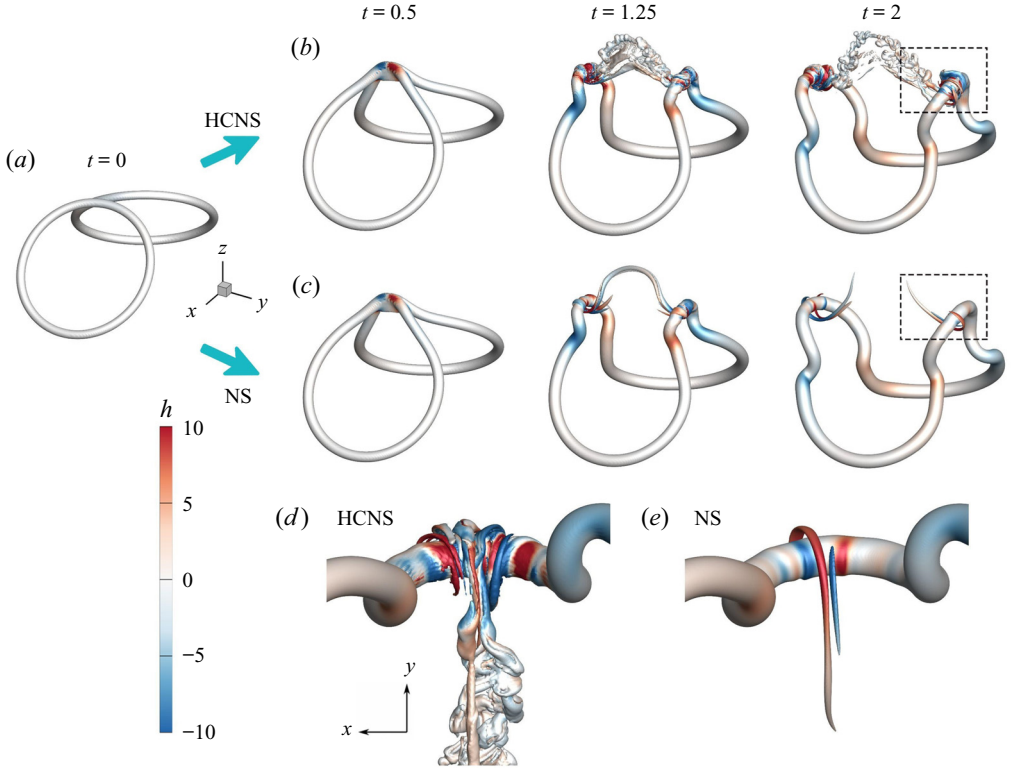

Figure 11. Evolution of the isosurface of $|\boldsymbol{\omega}| = 0.04\omega_0$ colour-coded by the helicity density for (*a*) the asymmetric collision of vortex rings in (*b*) HCNS and (*c*) NS flows. Close-up views of vortical structures at $t = 2$ after asymmetric reconnection in (*d*) the HCNS flow and (*e*) the NS flow. The zoom-in regions are marked by dashed boxes in (*b*) and (*c*), respectively.

5.4. *Decaying HIT*

We compare HCNS and NS dynamics in decaying HIT. Figure 13 compares the total kinetic energy, enstrophy, helicity and Beltramization criterion in HCNS and NS flows. At early times $t \leq O(1)$, the evolutions of E and Ω in HCNS and NS flows are close; $\mathcal{H}$ starts to grow in the NS flow; and Λ_B of the two flows are almost identical. Note that

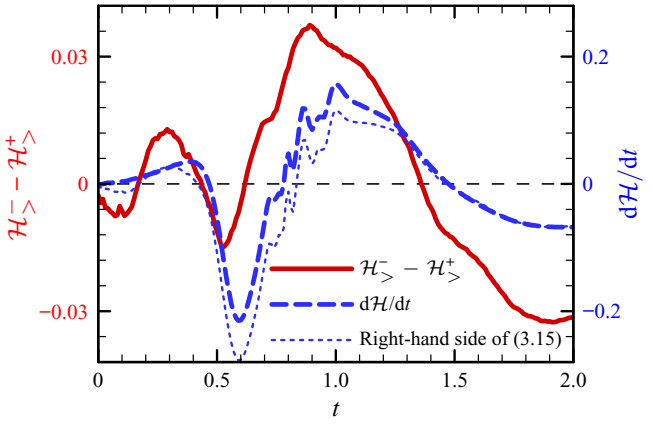

Figure 12. Evolution of the difference between left- and right-handed helicity components at small scales, the time rate of helicity and right-hand side of (3.15) during the asymmetric collision of vortex rings in the NS flow.

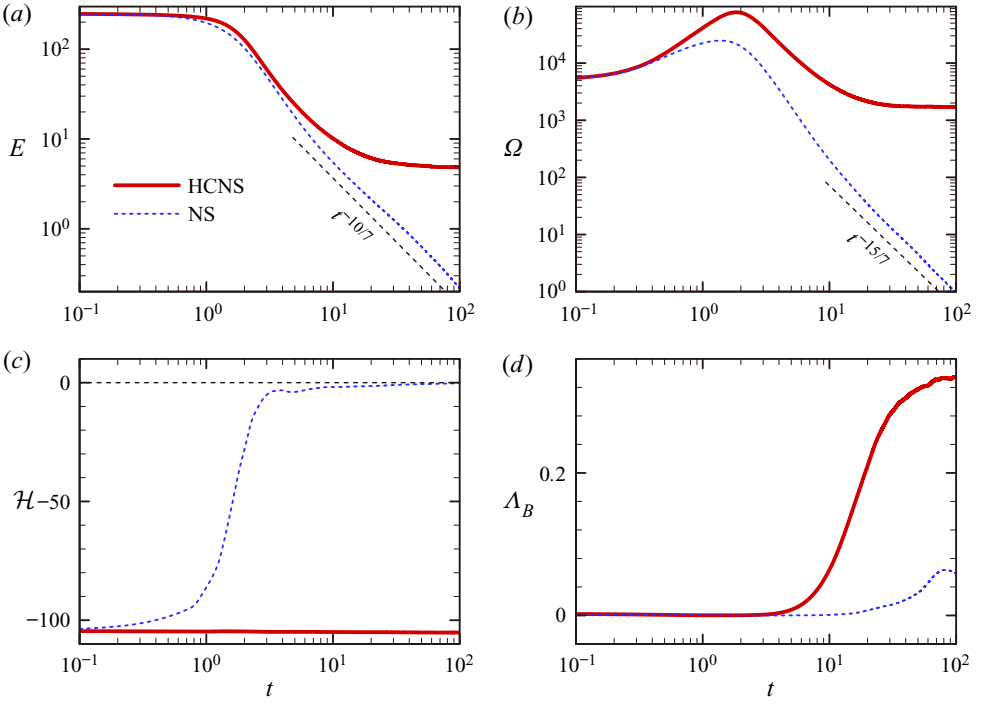

Figure 13. Evolution of (*a*) total kinetic energy, (*b*) enstrophy, (*c*) helicity and (*d*) Beltramization criterion for decaying HIT at $Re = 500$ in HCNS and NS flows.

the initial helicity is determined by the initial Gaussian random field with a generator of random numbers, so it varies in different realizations, i.e. $\mathcal{H}_0$ can be either positive or negative. From contours of the helicity density in figure 14(*b*,*e*), the large-scale structures in both flows are also similar, and some local $|h|$ in the HCNS flow is larger than that in the NS flow.

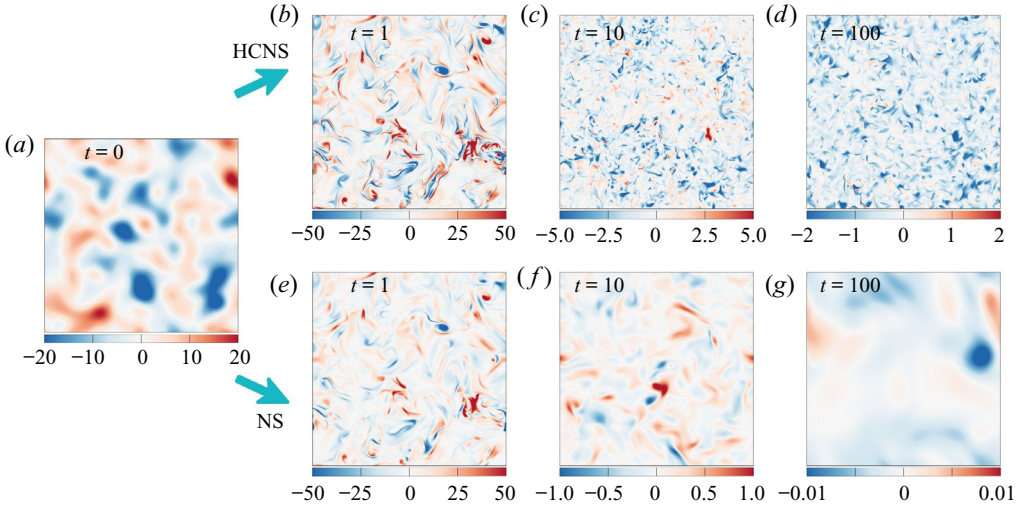

Figure 14. Evolution of the helicity-density contour on the x–y plane at $z = \pi$ for (a) decaying HIT at $Re = 500$ in (b–d) HCNS and (e–g) NS flows.

At later times $t > O(1)$, HCNS and NS dynamics behave very differently. In figures 13(a) and 13(b), $E \sim t^{-10/7}$ and $\Omega \sim t^{-15/7}$ decay with the Kolmogorov decaying laws (Kolmogorov 1941) at late times in the NS flow. By contrast, E and Ω in the HCNS flow slowly decay and relax to constants E_∞ and Ω_∞ in (2.38), respectively. The helicity remains invariant in the HCNS flow, whereas it relaxes to zero in the NS flow. In particular, the HCNS flow exhibits much stronger Beltramization, as the faster and larger growth of Λ_B, than the NS flow. A complete Beltramization of HIT in the HCNS flow, i.e. $\Lambda_B \to 1$ implied from (2.38), appears to be very slow at late times.

The Beltramization of HIT in the HCNS flow is visualized in figure 14. The initial parity asymmetry due to the random initial field grows with time in the HCNS flow, as illustrated by the dominance of negative h at $t = 10$ and 100 in figure 14(c,d). In contrast, the parity symmetry is restored at long times due to the viscous decay in the NS flow. Furthermore, the small-scale structures are remarkably maintained at late times in the dissipative HCNS flow without external forces, while they are gradually dissipated in the NS flow. In figure 15(a), the right-handed helicity component goes to zero while the left-handed one remains constant at $t \geq O(10^2)$ in the HCNS flow, and $\mathcal{H}^{\pm}_{\mathrm{HCNS}} > \mathcal{H}^{\pm}_{\mathrm{NS}}$ is consistent with (3.38). Thus, the HCNS equation seems natural to generate purely chiral turbulence (Biferale *et al.* 2013).

For the decaying HIT, we take

$$\mathcal{L} = \frac{\pi}{2u'^2} \int_0^\infty \frac{E_k(k)}{k}\, \mathrm{d}k \tag{5.5}$$

as the integral length scale and $\mathcal{U} = u' = (2\langle E\rangle/3)^{1/2}$ as the root-mean-square velocity. The truncated wavenumber in (3.13) becomes

$$k_c(t) = \frac{\nu^{-1/3}}{2 \times 3^{5/6}\pi^{19/6}} E^{5/6}(t) \left(\int_0^\infty \frac{E_k(k)}{k}\, \mathrm{d}k \right)^{-2/3}, \tag{5.6}$$

which initially is $k_c(0) \approx 10.2$ at $Re = 500$ and slightly increases then decreases with time. Figure 15(b) compares evolutions of $E_k(k)$ in HCNS and NS flows, where k_c at different

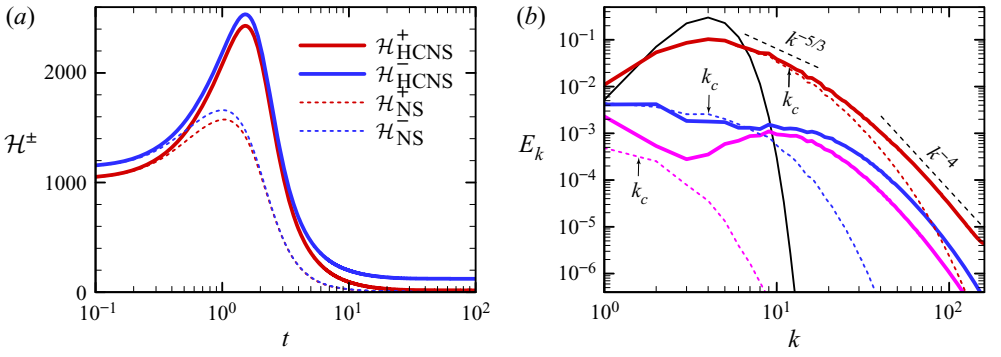

Figure 15. (*a*) Evolution of the left- and right-handed helicity components and (*b*) energy spectra at $t = 0$ (black), 1 (red), 10 (blue) and 100 (magenta) for decaying HIT in HCNS and NS flows. Solid and dashed lines denote the profiles in HCNS and NS flows, respectively, and k_c for the NS flow is marked near the profiles of E_k at different times.

times are marked by arrows. The spectra broaden with time, indicating energy cascade, and have a narrow inertial range with the $-5/3$ scaling law in both flows. The inertial range is expected to be wider with increasing Re. At later times, $E_k(k)$ at high k in the HCNS flow is significantly larger than that in the NS flow. In particular, $E_k(k)$ in the dissipation range in this HIT and other HCNS flow (see figure 7*b*) shows a k^{-4} law at late times, which seems related to the Beltramization of the HCNS flow at small scales.

A similar scaling law of k^{-4} was reported in the anisotropic kinetic alpha instability (Sulem *et al.* 1989) and the near-maximum helical turbulent state (Plunian *et al.* 2020), and a scaling law of $k^{-7/3}$ was observed in the evolution of a pair of anti-parallel strongly polarized vortex tubes (Yao & Hussain 2021).

6. Conclusions

We propose the HCNS equation (2.8) by modifying the non-ideal force term in the NS equation (2.2). The corresponding HCNS flow has strict helicity conservation in (2.29) and finite dissipation in (2.18). We find that, in general, the imposed helicity conservation has very minor influence on the evolutionary topology and geometry of large-scale structures, whereas it has an impact on those of small-scale structures.

We theoretically derive several properties of the HCNS flow. In (2.25), the enstrophy of the HCNS flow is larger than that of the NS flow from the same initial condition. In (2.38), the HCNS flow tends to be Beltramized at long times. In (3.27), the pentadic mode interactions in the HCNS dynamics are more complex than the triadic interactions in the NS dynamics. In (3.38), the left- and right-handed helicity components in the HCNS flow are larger than their counterparts in the NS flow. Furthermore, we demonstrate in (3.21) that parity breaking at small scales can trigger a notable time variation of helicity in the NS flow.

The comparative DNS study of HCNS and NS flows elucidates the influence of helicity conservation on flow structures and statistics. First, the flow with helicity conservation has the ultimate Beltrami state. In the evolution of the twisted vortex ring, the twisted vortex lines are preserved in the HCNS flow while they become parallel in the NS flow at long times. In decaying HIT, small-scale flow structures with positive or negative helicity density are preserved, and the energy spectra show a k^{-4} scaling law in the dissipation

range in the HCNS flow. Thus, the HCNS equation is natural to generate a purely chiral turbulent flow (Biferale *et al.* 2012, 2013).

Second, large-scale flow structures are similar and small-scale structures are different in the evolution of HCNS and NS flows from the same initial condition. During vortex reconnection of the trefoil vortex knot and the asymmetric collision of vortex rings, the geometries and topologies of vortex core lines in HCNS and NS flows are almost identical. This indicates that the helicity can be invariant during significant topological changes of vortices by altering internal structures of vortex tubes. On the other hand, many more small-scale threads are generated in the HCNS flow than in the NS flow, consistent with the slower energy decay and the k^{-4} scaling of $E_k(k)$ in the dissipation range in the HCNS flow.

Moreover, the symmetry breaking of left- and right-handed structures at small scales, with finite $|\mathcal{H}^+_> - \mathcal{H}^-_>|$, during vortex reconnection can lead to a notable helicity variation in the NS flow. In turn, the imposed helicity conservation generates extra threads via the pentadic mode interactions to make a delicate balance of $\mathcal{H}^+$ and $\mathcal{H}^-$, and thus keep absolute parity symmetry for flows with $\mathcal{H}_0 = 0$. The findings above hint that helicity may not be conserved in the inviscid limit of NS flows, because parity breaking at small scales seems to be unavoidable in practical flows under various disturbances and instabilities.

In future work, the theoretical framework of the HCNS flow can be extended to study helicity conservation in the inviscid limit, the mechanism of energy and helicity cascades and the flow control with manipulation of parity symmetry at small scales.

Acknowledgements. Numerical simulations and visualization were carried out on the Tianhe-2A supercomputer in Guangzhou, China.

Funding. This work has been supported in part by the National Natural Science Foundation of China (grant nos. 11925201, 91952108 and 11988102), the National Key R&D Program of China (no. 2020YFE0204200) and the Xplore Prize.

Declaration of interests. The authors report no conflict of interest.

Author ORCIDs.
Zhaoyuan Meng https://orcid.org/0000-0002-0933-4272;
Weiyu Shen https://orcid.org/0000-0003-4385-8835;
Yue Yang https://orcid.org/0000-0001-9969-7431.

Appendix A. Helicity variation under small-scale parity breaking

Equation (3.15) implies that parity breaking at small scales can lead to a notable helicity variation. Their causality is investigated by perturbing a vortex ring at small scales, i.e. imposing an asymmetric disturbance with $k > k_c$ to a symmetric vortex with $\mathcal{H}_0 = W_{r0} = T_{w0} = 0$. Here, k_c is defined in (5.1), and values of R_0, r_0, p and q are the same as those in the DNS of the twisted ring. The evolution of an unperturbed vortex ring in an unbounded viscous flow has $\mathcal{H} = 0$ for all times.

In the numerical experiment with $Re = 2000$, we artificially impose a small-scale disturbance on the left-handed velocity mode in Fourier space at $t = t_d$ as

$$u^-(\boldsymbol{k}, t = t_d^+) = \left(1 + 2\exp\left[\frac{-(k - 2k_c)^4}{100k_c^2}\right]\right) u^-(\boldsymbol{k}, t = t_d^-), \tag{A1}$$

after the vortex ring evolves for a short time $t_d = 2$ in the NS flow.

The perturbation (A1) amplifies $\mathcal{H}^-_k$ near $k = 2k_c$ to break parity symmetry at small scales in figure 16(*a*), and it only adds a negligible amount of energy at small scales

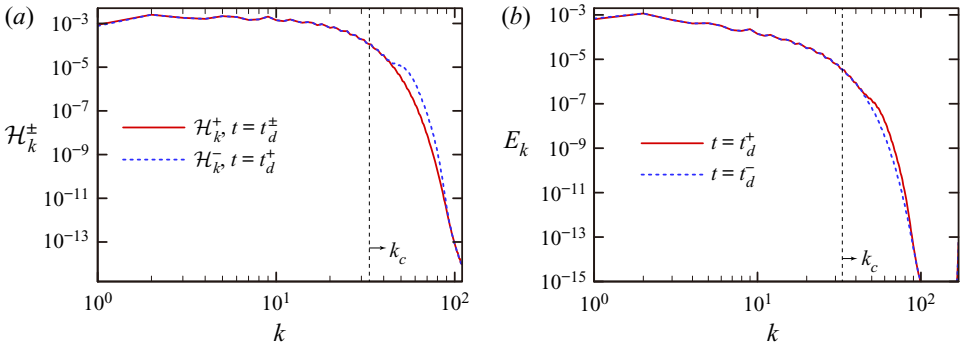

Figure 16. (*a*) Left- and right-handed helicity spectra after small-scale perturbation imposed on the vortex ring at $t = t_d$. (*b*) Energy spectra after ($t = t_d^+$) and before ($t = t_d^-$) the perturbation.

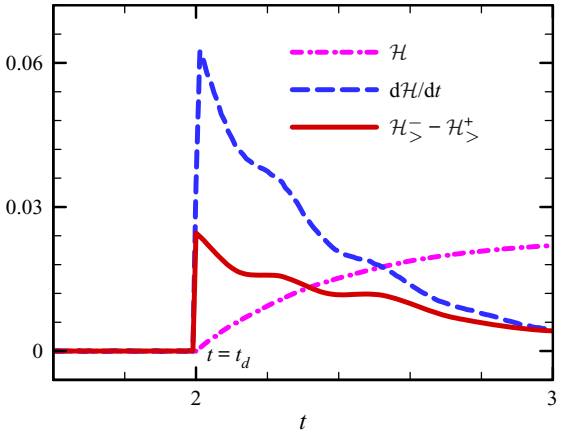

Figure 17. Evolution of the helicity, the time rate of helicity and the difference between small-scale left- and right-handed helicity components for the vortex ring perturbed at $t = t_d$.

in figure 16(*b*). In the meantime, we slightly lower the amplitude of the left-handed component at the largest scale as

$$u^-(\boldsymbol{k}, t = t_d^+)|_{k=1} = 0.775 u^-(\boldsymbol{k}, t = t_d^-)|_{k=1} \tag{A2}$$

to keep $\mathcal{H}(t_d^+) = \mathcal{H}(t_d^-) = 0$. Note that the perturbation performed in the normal plane of $\boldsymbol{k}$ keeps the perturbed velocity incompressible.

In figure 17, the imposed $\mathcal{H}_>^- - \mathcal{H}_>^+ > 0$ at $t = t_d$ causes $\mathrm{d}\mathcal{H}/\mathrm{d}t$ to surge to a finite value, and $\mathcal{H}$ begins to grow after $t = t_d$. Moreover, the difference of $E(t)$ in flows with or without the disturbance is negligible. Figure 18 illustrates the evolution of the contour of a normalized helicity density in the y–z plane at a cross-section of the vortex ring. At $t = t_d^+$, the negative helicity density is concentrated at the vortex core due to the enhancement of the energy for small-scale left-handed structures. In the subsequent evolution, large-scale right-handed spiral structures form with $\mathcal{H} > 0$, similar to the observation in Takaoka (1996). Hence, it is evident that parity breaking at small scales can trigger a notable time variation of helicity in the NS flow.

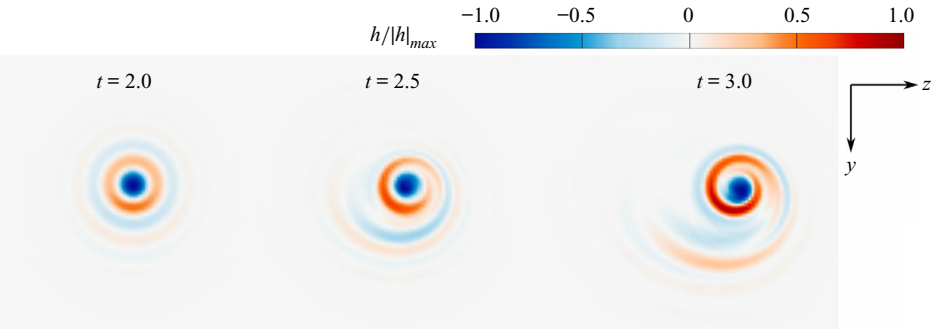

Figure 18. Evolution of the contour of the helicity density normalized by $|h|_{\max}(t)$ on the y–z plane at $x = \pi$ for the perturbed vortex ring. Note that the other half of the cross-section is not shown due to axial symmetry with respect to $x = y = 0$.

References

Alexakis, A. 2017 Helically decomposed turbulence. *J. Fluid Mech.* **812**, 752–770.

Alexakis, A. & Biferale, L. 2018 Cascades and transitions in turbulent flows. *Phys. Rep.-Rev. Sec. Phys. Lett.* **767–769**, 1–101.

Alexakis, A. & Biferale, L. 2022 λ–Navier–Stokes turbulence. *Phil. Trans. R. Soc.* A-*Math. Phys. Engng Sci.* **380**, 20210243.

André, J.C. & Lesieur, M. 1977 Influence of helicity on the evolution of isotropic turbulence at high Reynolds number. *J. Fluid Mech.* **81**, 187–207.

Arnold, V.I. 1992 Topological methods in hydrodynamics. *Annu. Rev. Fluid Mech.* **24**, 145–166.

Arnold, V.I. 2014 *The Asymptotic Hopf Invariant and its Applications*, pp. 357–375. Springer Berlin Heidelberg.

Batchelor, G.K. 1953 *The Theory of Homogeneous Turbulence*. Cambridge University Press.

Biferale, L., Musacchio, S. & Toschi, F. 2012 Inverse energy cascade in three-dimensional isotropic turbulence. *Phys. Rev. Lett.* **108**, 164501.

Biferale, L., Musacchio, S. & Toschi, F. 2013 Split energy-helicity cascades in three-dimensional homogeneous and isotropic turbulence. *J. Fluid Mech.* **730**, 309–327.

Biferale, L. & Titi, E.S. 2013 On the global regularity of a helical-decimated version of the 3D Navier–Stokes equations. *J. Stat. Phys.* **151**, 1089–1098.

Bos, W.J.T. 2021 Three-dimensional turbulence without vortex stretching. *J. Fluid Mech.* **915**, A121.

Briard, A. & Gomez, T. 2017 Dynamics of helicity in homogeneous skew-isotropic turbulence. *J. Fluid Mech.* **821**, 539–581.

Brissaud, A., Frisch, U., Leorat, J., Lesieur, M. & Mazure, A. 1973 Helicity cascades in fully developed isotropic turbulence. *Phys. Fluids* **16**, 1366–1367.

Chen, Q., Chen, S. & Eyink, G.L. 2003*a* The joint cascade of energy and helicity in three-dimensional turbulence. *Phys. Fluids* **15**, 361–374.

Chen, Q., Chen, S., Eyink, G.L. & Holm, D.D. 2003*b* Intermittency in the joint cascade of energy and helicity. *Phys. Rev. Lett.* **90**, 214503.

Constantin, P. & Majda, A. 1988 The Beltrami spectrum for incompressible fluid flows. *Commun. Math. Phys.* **115**, 435–456.

Devenport, W.J., Rife, M.C., Liapis, S.I. & Follin, G.J. 1996 The structure and development of a wing-tip vortex. *J. Fluid Mech.* **312**, 67–106.

Ditlevsen, P.D. & Giuliani, P. 2001 Dissipation in helical turbulence. *Phys. Fluids* **13**, 3508–3509.

Frisch, U. 1995 *Turbulence: The Legacy of A. N. Kolmogorov*. Cambridge University Press.

Gallavotti, G. 1996 Equivalence of dynamical ensembles and Navier–Stokes equations. *Phys. Lett.* A **223**, 91–95.

Gallavotti, G. 1997 Dynamical ensembles equivalence in fluid mechanics. *Physica* D **105**, 163–184.

Hall, P. & Sherwin, S. 2010 Streamwise vortices in shear flows: harbingers of transition and the skeleton of coherent structures. *J. Fluid Mech.* **661**, 178–205.

Hao, J., Xiong, S. & Yang, Y. 2019 Tracking vortex surfaces frozen in the virtual velocity in non-ideal flows. *J. Fluid Mech.* **863**, 513–544.

Hussain, F. 1986 Coherent structures and turbulence. *J. Fluid Mech.* **173**, 303–356.

ISHIDA, T., DAVIDSON, P.A. & KANEDA, Y. 2006 On the decay of isotropic turbulence. *J. Fluid Mech.* **564**, 455–475.

JACCOD, A. & CHIBBARO, S. 2021 Constrained reversible system for Navier–Stokes turbulence. *Phys. Rev. Lett.* **127**, 194501.

KANEDA, Y., ISHIHARA, T., ITAKURA, K. & UNO, A. 2003 Energy dissipation rate and energy spectrum in high resolution direct numerical simulations of turbulence in a periodic box. *Phys. Fluids* **15**, 21–24.

KERR, R.M. 2018 Trefoil knot timescales for reconnection and helicity. *Fluid Dyn. Res.* **50**, 011422.

KIDA, S. & TAKAOKA, M. 1987 Bridging in vortex reconnection. *Phys. Fluids* **30**, 2911–2914.

KIDA, S. & TAKAOKA, M. 1988 Reconnection of vortex tubes. *Fluid Dyn. Res.* **3**, 257–261.

KIDA, S. & TAKAOKA, M. 1994 Vortex reconnection. *Annu. Rev. Fluid Mech.* **26**, 169–177.

KLECKNER, D. & IRVINE, W.T.M. 2013 Creation and dynamics of knotted vortices. *Nat. Phys.* **9**, 253–258.

KOLMOGOROV, A.N. 1941 On degeneration of isotropic turbulence in an incompressible viscous liquid. *Dokl. Akad. Nauk SSSR* **31**, 538–540.

KRAICHNAN, R.H. 1970 Diffusion by a random velocity field. *Phys. Fluids* **13**, 22–31.

KURGANSKY, M.V. 2017 Helicity in dynamic atmospheric processes. *Izv. Acad. Nauk SSSR Atmos. Ocean. Phys.* **53**, 127–141.

LAING, C.E., RICCA, R.L. & SUMNERS DE, W.L. 2015 Conservation of writhe helicity under anti-parallel reconnection. *Sci. Rep.* **5**, 9224.

MOFFATT, H.K. 1969 The degree of knottedness of tangled vortex lines. *J. Fluid Mech.* **35**, 117–129.

MOFFATT, H.K. 2014 Helicity and singular structures in fluid dynamics. *Proc. Natl Acad. Sci. USA* **111**, 3663–3670.

MOFFATT, H.K. 2017 Helicity – invariant even in a viscous fluid. *Science* **357**, 448–449.

MOFFATT, H.K. 2021 Some topological aspects of fluid dynamics. *J. Fluid Mech.* **914**, P1.

MOFFATT, H.K. & RICCA, R.L. 1992 Helicity and the Călugăreanu invariant. *Proc. R. Soc.* A-*Math. Phys. Engng Sci.* **439**, 411–429.

MOFFATT, H.K. & TSINOBER, A. 1992 Helicity in laminar and turbulent flow. *Annu. Rev. Fluid Mech.* **24**, 281–312.

MOREAU, J.J. 1961 Constantes d'un îlot tourbillonnaire en fluide parfait barotrope. *C. R. Acad. Sci. Paris* **252**, 2810–2812.

PELZ, R.B., SHTILMAN, L. & TSINOBER, A. 1986 The helical nature of unforced turbulent flows. *Phys. Fluids* **29**, 3506.

PLUNIAN, F., TEIMURAZOV, A., STEPANOV, R. & VERMA, M.K. 2020 Inverse cascade of energy in helical turbulence. *J. Fluid Mech.* **895**, A13.

POPE, S.B. 2000 *Turbulent Flows*. Cambridge University Press.

RICCA, R.L., SAMUELS, D.C. & BARENGHI, C.F. 1999 Evolution of vortex knots. *J. Fluid Mech.* **391**, 29–44.

RUAN, S., XIONG, S., YOU, J. & YANG, Y. 2022 Generation of streamwise helical vortex loops via successive reconnections in early pipe transition. *Phys. Fluids* **34**, 054112.

SAHOO, G., ALEXAKIS, A. & BIFERALE, L. 2017 Discontinuous transition from direct to inverse cascade in three-dimensional turbulence. *Phys. Rev. Lett.* **118**, 164501.

SCHEELER, M.W., KLECKNER, D., PROMENT, D., KINDLMANN, G.L. & IRVINE, W.T. 2014 Helicity conservation by flow across scales in reconnecting vortex links and knots. *Proc. Natl Acad. Sci. USA* **111**, 15350–15355.

SHE, Z.-S. & JACKSON, E. 1993 Constrained Euler system for Navier–Stokes turbulence. *Phys. Rev. Lett.* **70**, 1255–1258.

SHEN, W., YAO, J., HUSSAIN, F. & YANG, Y. 2022 Topological transition and helicity conversion of vortex knots and links. *J. Fluid Mech.* **943**, A41.

SLOMKA, J. & DUNKEL, J. 2017 Spontaneous mirror-symmetry breaking induces inverse energy cascade in 3D active fluids. *Proc. Natl Acad. Sci. USA* **114**, 2119–2124.

SREENIVASAN, K.R. 1984 On the scaling of the turbulence energy dissipation rate. *Phys. Fluids* **27**, 1048–1051.

SREENIVASAN, K.R. 1998 An update on the dissipation rate in homogeneous turbulence. *Phys. Fluids* **10**, 528–529.

SULEM, P.L., SHE, Z., SCHOLL, H. & FRISCH, U. 1989 Generation of large-scale structures in three-dimensional flow lacking parity-invariance. *J. Fluid Mech.* **205**, 341–358.

TAKAOKA, M. 1996 Helicity generation and vorticity dynamics in helically symmetric flow. *J. Fluid Mech.* **319**, 125–149.

TAYLOR, G.I. & GREEN, A.E. 1937 Mechanism of the production of small eddies from large ones. *Proc. R. Soc. Lond.* A-*Math. Phys. Engng Sci.* **158**, 499–521.

TONG, W., YANG, Y. & WANG, S. 2020 Characterizing three-dimensional features of vortex surfaces in the flow past a finite plate. *Phys. Fluids* **32**, 011903.
TRUESDELL, C. 2018 *The Kinematics of Vorticity*. Courier Dover Publications.
TSINOBER, A. & LEVICH, E. 1983 On the helical nature of three-dimensional coherent structures in turbulent flows. *Phys. Lett.* A **99A**, 321–324.
WALEFFE, F. 1992 The nature of triad interactions in homogeneous turbulence. *Phys. Fluids* **4**, 350–363.
WOLTJER, L. 1958 A theorem on force-free magnetic fields. *Proc. Natl Acad. Sci. USA* **44**, 489–491.
WOOD, D.H., MEHTA, R.D. & KOH, S.G. 1992 Structure of a swirling turbulent mixing layer. *Exp. Therm. Fluid Sci.* **5**, 196–202.
WU, J., MA, H. & ZHOU, M. 2015 *Vortical Flows*. Springer.
XIONG, S. & YANG, Y. 2019*a* Construction of knotted vortex tubes with the writhe-dependent helicity. *Phys. Fluids* **31**, 047101.
XIONG, S. & YANG, Y. 2019*b* Identifying the tangle of vortex tubes in homogeneous isotropic turbulence. *J. Fluid Mech.* **874**, 952–978.
XIONG, S. & YANG, Y. 2020 Effects of twist on the evolution of knotted magnetic flux tubes. *J. Fluid Mech.* **895**, A28.
YAN, Z., LI, X., YU, C., WANG, J. & CHEN, S. 2020 Dual channels of helicity cascade in turbulent flows. *J. Fluid Mech.* **894**, R2.
YANG, Y.-T., SU, W.-D. & WU, J.-Z. 2010 Helical-wave decomposition and applications to channel turbulence with streamwise rotation. *J. Fluid Mech.* **662**, 91–122.
YANG, Y.-T. & WU, J.-Z. 2011 Channel turbulence with spanwise rotation studied using helical wave decomposition. *J. Fluid Mech.* **692**, 137–152.
YAO, J. & HUSSAIN, F. 2021 Polarized vortex reconnection. *J. Fluid Mech.* **922**, A19.
YAO, J. & HUSSAIN, F. 2022 Vortex reconnection and turbulence cascade. *Annu. Rev. Fluid Mech.* **54**, 317–347.
YAO, J., SHEN, W., YANG, Y. & HUSSAIN, F. 2022 Helicity dynamics in viscous vortex links. *J. Fluid Mech.* **944**, A41.
YAO, J., YANG, Y. & HUSSAIN, F. 2021 Dynamics of a trefoil knotted vortex. *J. Fluid Mech.* **923**, A19.
ZHAO, X. & SCALO, C. 2021 Helicity dynamics in reconnection events of topologically complex vortex flows. *J. Fluid Mech.* **920**, A30.
ZHAO, Y., YANG, Y. & CHEN, S. 2016 Vortex reconnection in the late transition in channel flow. *J. Fluid Mech.* **802**, R4.
ZHAO, X., YU, Z., CHAPELIER, J. & SCALO, C. 2021 Direct numerical and large-eddy simulation of trefoil knotted vortices. *J. Fluid Mech.* **910**, A31.
ZHU, J., YANG, W. & ZHU, G. 2014 Purely helical absolute equilibria and chirality of (magneto) fluid turbulence. *J. Fluid Mech.* **739**, 479–501.